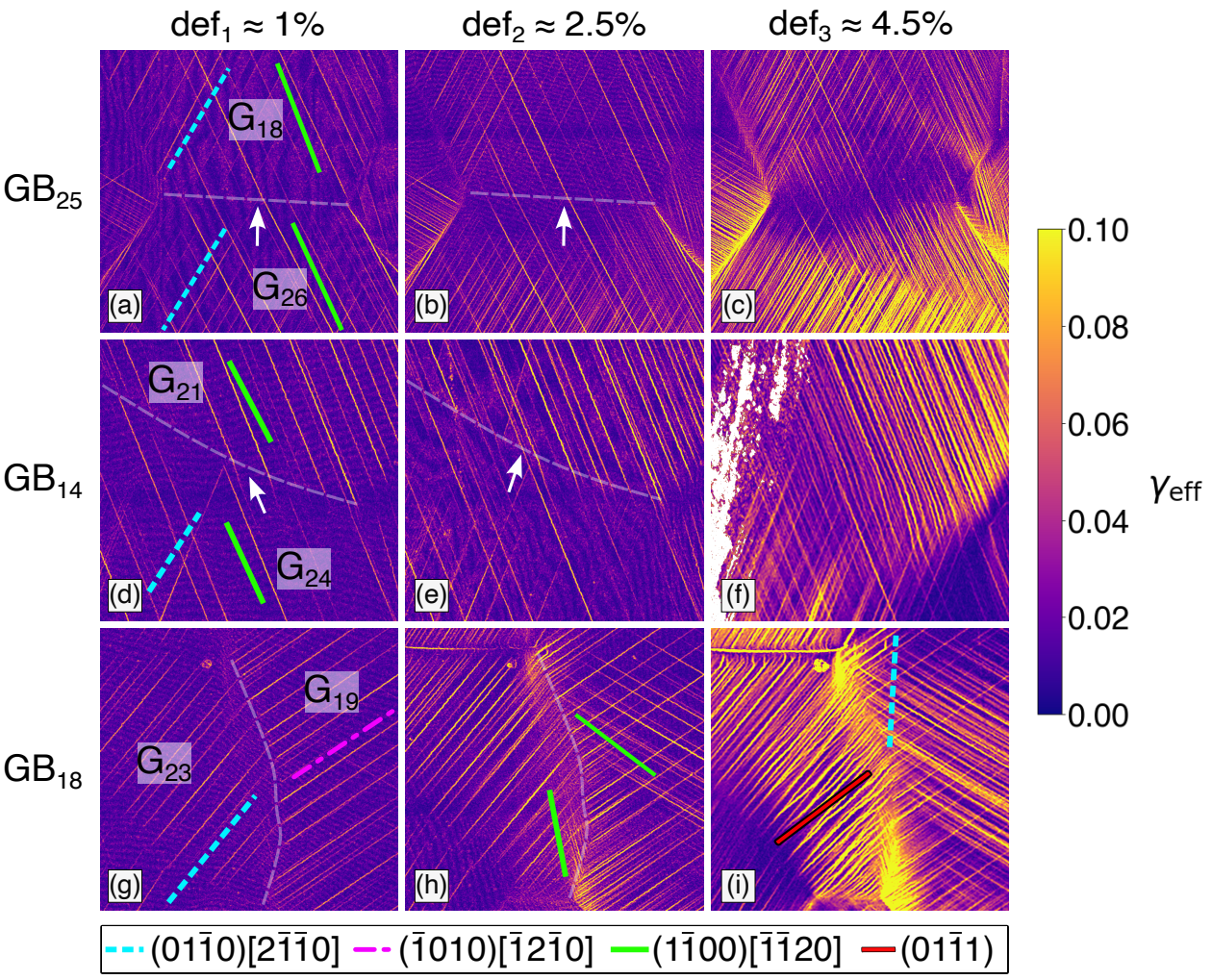

Figure 5.10: Effective shear strain maps after 1%, 2.5%, and 4.5% plastic deformation in the neighborhood of three GBs that do not fulfill the classical slip transfer criteria. (a), (b), and (c): GB_{25}. (d), (e), and (f): GB_{14}. (g), (h), and (i): GB_{18}. The theoretical prismatic slip traces of the observed active slip systems have been drawn for each GB, and the GB trace has been indicated with a fine dashed gray line at the first deformation map. An additional first-order pyramidal theoretical slip trace has been added in G_{23}.

fer does not progress between the blue slip bands even though these slip systems are well aligned. This difference in the slip transmission behavior may be attributed to the difference between the twist angles θ between the active pairs of prismatic slip systems ($\theta = 16.5°$ for the blue $(01\bar{1}0)[2\bar{1}\bar{1}0]$ versus $\theta = 5.1°$ for the green $(1\bar{1}00)[\bar{1}\bar{1}20]$ slip systems), which might favor slip transfer along the $(1\bar{1}00)[\bar{1}\bar{1}20]$ slip systems. There is an evident rise in the number of active slip bands in both grains at 4.5% deformation in both prismatic slip systems (Fig. 5.10 (c)), as well as significant strain concentrations at the neighbor GBs at the sides of G_{26}. Nonetheless, there is a lack of shear strain at the GB_{25} region and a limited number of visible shear bands going through it, in contrast to its neighborhood. Hence, the lack of slip transfer events between the pairs of active slip systems may be

attributed to the local strain heterogeneity, which locally reduces the driving force for slip. Both blue-to-blue and green-to-green prismatic slip transfer across GB_{25} seemed, in principle, very likely. However, the reduction in the effective shear strain, together with the absence of slip bands at the GB region, reveals that resolved shear stress for dislocation slip was very low near the GB, hindering slip transfer.

Table 5.2: Geometrical parameters and slip transfer criteria between the active prismatic slip systems for GB_{25}, GB_{14}, and GB_{18}. The rank of the SF of the active prismatic slip system among the three possible planes is indicated between parenthesis, and the SF is colored according to the active slip system indicated in the legend in Fig. 5.10.

GB_i	G_A	G_B	$SF_A(R)$	$SF_B(R)$	Θ	κ	ψ	θ	m'	$\Delta b/b$	LRB
GB_{25}	18	26	0.47(1)	0.46(1)	11.7°	7.6°	9.2°	16.5°	0.98	0.13	0.95
GB_{25}	18	26	0.38(2)	0.4(2)	11.7°	11.6°	2.9°	5.1°	0.98	0.2	0.98
GB_{14}	21	24	0.44(1)	0.37(2)	17.3°	11.2°	15.2°	17.8°	0.95	0.2	0.93
GB_{18}	19	23	0.43(2)	0.5(1)	15°	14.2°	14.8°	9.5°	0.94	0.25	0.96

GB_{14} presents partial slip transfer between green $(1\bar{1}00)[\bar{1}\bar{1}20]$ prismatic slip systems from 1% plastic deformation. The slip activity in grains G_{21} and G_{24} is dominated by the highest SF for the first and second deformations (green prismatic), but with increasing activity of the blue prismatic slip system $(01\bar{1}0)[2\bar{1}\bar{1}0]$ (ranked first in SF) in G_{24} from 2.5% deformation. As observed in Fig. 5.10 (d), a few slip bands reach the boundary and then fade towards the interior of G_{24} as indicated by the white arrow, but with no extended slip transfer behavior throughout the length of GB_{14}. The geometrical alignment between the pair of green slip systems is rather good, as shown in Table 5.2, except for the θ angle, which might be slightly larger than that of other GBs. Nevertheless, several slip bands can go through the GB and penetrate through the neighbor grain at the second deformation (Fig. 5.10 (e)). In this case, the white arrow points at a slip band in G_{24} which was already present at 1% deformation, and that goes through GB_{14} at 2.5% towards G_{21}. Moreover, several new slip bands reach the boundary from G_{21} and clearly fade after going through it, as observed at the first deformation step. Finally, there is convincing slip transfer from green-to-green prismatic slip systems across GB_{14} at 4.5% plastic deformation (Fig. 5.10 (f)), which may be driven from G_{21} to G_{24} according to the gradient in the effective shear strain. This observation might also be supported by the fact that the green prismatic system in G_{21} has a higher SF than that of G_{24} (0.44 against 0.37), where it is ranked second. The $(01\bar{1}0)[2\bar{1}\bar{1}0]$ slip system activity increases in G_{24} (ranked first in SF with value 0.47) after 2.5% deformation and dominates at 4.5%, compared to the green prismatic slip system. This might cause the green-to-green slip transfer not to progress that much towards the interior of G_{24}, where the blue prismatic dominates over the green. In summary, the dominant prismatic slip systems (green in G_{21} and blue in G_{24}) are not properly aligned for slip transfer, in contrast to the green prismatic slip systems which are suitably aligned. However, partial slip transfer is observed until 4.5% applied deformation, where convincing slip transfer is finally observed. This may be attributed to a lack of driving force to transfer slip from a dominant to a non-dominant slip system at low strains.

The case of GB_{18} is somewhat different from the previous two cases since there is convincing slip transfer between the blue $(01\bar{1}0)[2\bar{1}\bar{1}0]$ in G_{23} and the pink $(\bar{1}010)[\bar{1}2\bar{1}0]$ in G_{19} prismatic slip systems from the lowest deformation. The SF of the involved slip systems are both high (> 0.43), and the geometrical alignment is excellent, as shown in Table 5.2. The slip transfer process between this pair of prismatic slip systems does not significantly change with the applied deformation. However, the location of GB_{18} within the region of the macro-strain band (Fig. 5.5) induces the activation of additional deformation mechanisms necessary to accommodate the local stress. After 2.5% plastic deformation, the green $(1\bar{1}00)[\bar{1}\bar{1}20]$ prismatic slip system is activated in G_{23} with SF 0.23 (ranked third) and in G_{19} with SF 0.43 (ranked first), as shown in Fig. 5.10 (h). In the former, the activation of this prismatic slip system seems unlikely owing to its low SF, and yet it appears as thin slip bands near the proximity of the triple junction at the bottom, where plastic deformation is accumulated. The strain concentrations that appear at the triple points and at the GB itself after the third deformation step give rise to the activation of other plastic deformation mechanisms (Fig. 5.10 (i)). The large plastic deformation in G_{23} induces the appearance of wavy slip bands that arise from the $(01\bar{1}0)[2\bar{1}\bar{1}0]$ prismatic traces, that correlate with the theoretical slip trace direction of the first-order pyramidal slip system $(01\bar{1}1)$. Two possible slip systems share this pyramidal plane, $[1\bar{2}13]$ with SF 0.31 and $[\bar{1}\bar{1}23]$ with SF 0.08, therefore the former could be assumed to be active. Slip transfer is not observed between the first-order pyramidal slip system and any slip system active in G_{19}. Moreover, L-shaped slip bands are observed near the top triple junction among G_{23}, G_{19}, and G_{22}. They are associated with a slip plane change between the pink and the blue (SF 0.006, ranked third) prismatic slip systems in G_{19}. Consequently, after 4.5% plastic deformation, three slip systems have been activated in each grain at each side of GB_{18} despite being considerably unlikely and caused by the large strain concentration in this area. In brief, the large local strains observed around GB_{18} lead to the activation of multiple slip systems regardless of their macroscopic SF to accommodate the high plastic deformation in the neighborhood.

Overall, the two GBs analyzed in Fig. 5.10 (GB_{25} and GB_{14}) do not fulfill the classical slip transfer geometrical criteria because the local stresses affect the driving force for slip transfer across the GB. This leads to the observation of either limited slip transfer events or even partial slip transfer that only evolves to convincing slip transfer when the applied deformation is sufficient to drive slip toward the adjacent grain. In contrast, GB_{18} illustrates that, even when slip transfer is clearly observed, it is not enough to accommodate the large plastic deformation, and other plastic deformation mechanisms emerge.

Two additional GBs have been analyzed to showcase to which extent the local stress distribution can affect the occurrence or absence of slip transfer across a GB. First, GB_{16} has been selected as an example of how slip transfer can be impeded by insufficient local stress despite the good alignment between the active slip systems. As shown in the first row of Fig. 5.11, the dominant slip systems in G_{25} and G_{23} are the blue prismatic $(01\bar{1}0)[2\bar{1}\bar{1}0]$ with the highest SF (> 0.47). These slip systems are very well aligned regarding the angles κ and ψ, while the twist angle θ is slightly higher ($20.7°$). This leads to high m' and LRB values and low $\Delta b/b$, which indicate a great probability of slip transfer between the active prismatic slip systems. However, slip transfer is not observed after 1% deformation,

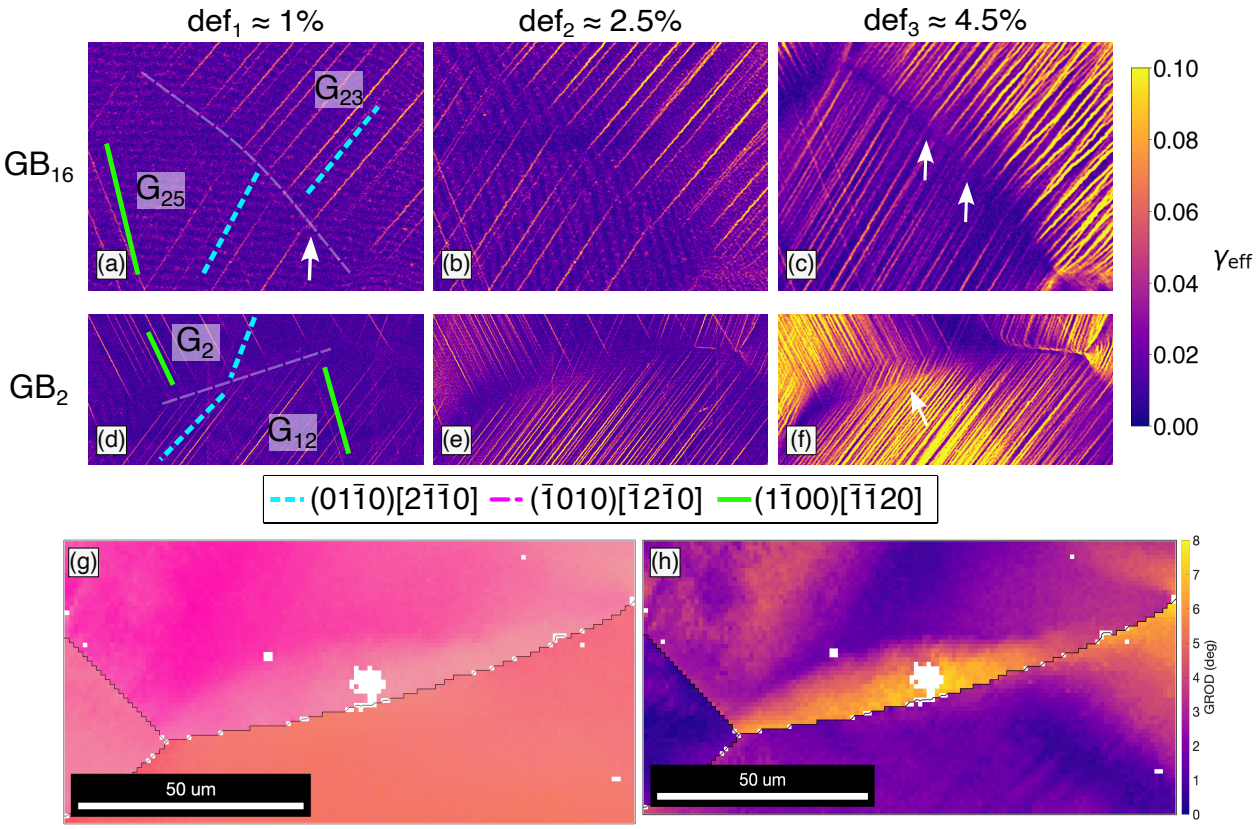

Figure 5.11: Detail shear strain HRDIC maps of two GBs that do not follow the classical slip transfer criteria. (a), (b), and (c): GB_{16} shear strain maps after 1%, 2.5%, and 4.5% plastic deformation, respectively. (d), (e), and (f): GB_2 shear strain maps after 1%, 2.5%, and 4.5% plastic deformation, respectively. For each GB, the theoretical prismatic slip traces of the observed active slip systems have been drawn, and the GB trace has been indicated with a translucent dashed gray line at the first deformation map. (g) and (h): G_2 EBSD and grain reference orientation deviation (GROD) maps after 4.5% plastic deformation, respectively.

Table 5.3: Geometrical parameters and slip transfer criteria between the active prismatic slip systems for GB_{16} and GB_2. The rank of the SF of the active prismatic slip system among the three possible planes is indicated between parenthesis, and the SF is colored according to the active slip systems indicated in the legend in Fig. 5.10.

GB_i	G_A	G_B	$SF_A(R)$	$SF_B(R)$	Θ	κ	ψ	θ	m'	$\Delta b/b$	LRB
GB_{16}	23	25	0.5(1)	0.47(1)	12.8°	11.9°	11.9°	20.7°	0.96	0.21	0.92
GB_2	12	2	0.5(1)	0.45(1)	61.4°	45.5°	40.5°	46.6°	0.53	0.77	0.48
GB_2	12	2	0.28(2)	0.41(2)	61.4°	58.1°	21.2°	36.1°	0.49	0.97	0.43

where only one trace matches across the GB but with a small curvature (indicated with a

white arrow in Fig. 5.11 (a)), suggesting that the continuity across the boundary may not be ideal. The slip band intensity increases in both grains at 2.5% plastic strain, but the number of active slip bands does not increase, and slip transfer is not yet clearly observed for any pair of bands (Fig. 5.11 (b)). After 4.5% plastic deformation, the slip activity in the prismatic blue slip systems significantly increases, and several instances of slip transfer across GB_{16} are observed, as highlighted by the white arrows in Fig. 5.11 (c). However, the continuity across the traces is not visible over the GB trace, which presents near-zero shear strain, suggesting that slip transfer across this GB might not be perfect. This may be attributed to insufficient local stresses to drive plastic deformation from one grain to the other, unlike those GBs located in other highly stressed regions.

Conversely, the local stresses could also assist the slip transfer process even if the slip systems across the GB are poorly aligned. The second row of Fig. 5.11 shows the effective shear strain distribution in GB_2, located within the macro-strain band region. As shown in Fig. 5.11 (d), there is double slip activation of the two highest SF prismatic slip systems in G_2 and G_{12}. The geometrical parameters and slip transfer criteria for the two pairs of prismatic slip systems (blue-to-blue and green-to-green) indicate that slip transfer across this GB would be unlikely due to their poor alignment (Table 5.3). Nevertheless, there are several visible blue-to-blue prismatic slip transfer events at 2.5% plastic deformation, and the process is possibly driven from G_{12} to G_2, given the intensity of the shear bands. At 4.5% deformation, there is convincing slip transfer between the blue prismatic slip systems across GB_2. The slip bands do not progress much through G_2 but extinguish a few microns away from the GB, where $(1\bar{1}00)[\bar{1}\bar{1}20]$ is dominant. Taking a closer look at the EBSD map acquired after 4.5% deformation (Fig. 5.11 (g)), it is clear that there is a local crystal rotation in G_2 close to GB_2. The grain reference orientation deviation (GROD) map is provided in Fig. 5.11 (h) as a measure of the misorientation between every pixel in the EBSD map and G_2 average orientation. The GROD distribution points out a significant crystal rotation near GB_2 of about 8°, probably caused by the large plastic deformation induced by the local stresses. This case proves that, even though the alignment between the active slip systems across a GB seems inadequate for slip transfer, large local stresses can provide enough driving force to overcome the GB energy barrier and induce slip transmission to the neighbor grain.

5.4 Conclusions

Slip transfer/blocking across 28 GBs was analyzed as a function of the applied plastic deformation in a pure Ti sample with strong rolling texture by means of slip trace analysis and high-resolution digital image correlation. The grain structure was determined in 3D using diffraction contrast tomography, so all the geometrical parameters that describe the alignment between the active slip systems across a grain boundary were known. Prismatic slip was practically the only plastic deformation mechanism, and the active prismatic slip systems presented high SF.

It was found that classical slip transfer geometrical criteria (m', Δb, or LRB) are generally good predictors for the likelihood of slip transmission across grain boundaries, indicating

that the probability of slip transfer across a grain boundary is strongly correlated with the geometrical alignment between the active slip systems. Thus, those grain boundaries where the active prismatic slip systems were well-aligned presented either full or partial slip transfer, and, conversely, slip blocking was observed when the alignment was poor. However, the information provided by high-resolution digital image correlation showed that local strain concentrations could affect the slip transfer process regardless of the geometrical alignment between the slip systems. In particular:

• Slip transfer between a pair of well-oriented slip systems can be impeded (leading to either partial slip transfer or even blocking) if there is another dominant slip system that is more favorable in terms of the SF to accommodate the plastic deformation across the boundary.

• Slip transfer between well-aligned slip systems across the boundary can be blocked as a result of the lack of driving force to transfer deformation due to the strain heterogeneity in the microstructure.

• Slip transfer may occur across a highly misoriented grain boundary due to the local stress concentrations, which provide sufficient driving force to overcome the energy barrier induced by the grain boundary and transmit dislocations to the adjacent grain.

In any case, despite the effect of the local stress concentrations, well-known slip transfer geometrical criteria, such as m', Δb, or LRB, can be used as a good first approximation for predicting slip transfer across grain boundaries. Moreover, these criteria can be easily implemented within the framework of crystal plasticity simulations of the mechanical behavior of polycrystals. This task will be accomplished in the following chapters.

6 Simulation of polycrystal deformation including slip transfer/blocking at grain boundaries

6.1 Introduction

The strength of pure metals is very low as a result of the development of plastic deformation by dislocation slip. Hence, they have to be strengthened by obstacles that hinder dislocation motion, and grain boundaries (GBs) stand among the strongest barriers to dislocation slip in polycrystals. As shown in previous chapters, the interaction of dislocations with GBs can be grouped into three categories. Opaque or impenetrable GBs do not allow the propagation of dislocation slip through the boundary, leading to the formation of dislocation pile-ups and local stress concentrations [26, 58]. Conversely, transparent GBs are found when all the active slip systems are suitably aligned, and the dislocations gliding in the incoming grain can be transmitted to the neighbor grain. Finally, dislocations in some active slip systems can easily propagate through the boundary, while others are blocked in the case of translucent GBs. This phenomenon leads to stress concentrations at the GB that depend on the number and intensity of slip in the systems blocked at the GB.

The effect of GBs on the strength of polycrystals was recognized in the 1950s, leading to the phenomenological Hall-Petch law [72, 143] that relates the yield strength of the polycrystal, σ_y with the average grain size, $\bar{D}_g$, according to

$$\sigma_y = \sigma_\infty + C_{HP}\,\bar{D}_g^{-x} \tag{6.1}$$

where σ_∞ is the yield stress of a polycrystal with very large grain size, C_{HP} a material constant and x a scaling exponent in the range -0.5 to -1 [47, 48, 112, 147].

Understanding the mechanical behavior of polycrystals has progressed rapidly in recent years through the combination of computational homogenization and crystal plasticity constitutive models [158]. As explained in Section 1.4, two different strategies have been used to study the effect of GBs on the strength of polycrystals based on either strain-gradient or physically-based crystal plasticity models. In the context of physically-based models, Haouala *et al.* [77] determined the effect of grain size on the strength of different

FCC polycrystals by means of computational homogenization of RVEs containing several hundred grains using a Fast Fourier Transform in combination with a strain gradient crystal plasticity model. The simulation results were in good agreement with the experimental data for Cu, Al, Ag, and Ni polycrystals for grain sizes $> 20\ \mu m$. Similar results were also obtained by Rubio *et al.* [151] through computational homogenization of equivalent RVEs using the finite element method and a physically-based crystal plasticity model that takes into account the storage of dislocations near the grain boundaries, following the approach developed by Haouala *et al.* [78]. Interestingly, the predictions of the physically-based model also overestimated the strength of the polycrystals when the average grain size was $< 20\ \mu m$. It was argued that the differences between experimental data and simulation results (using either strain gradient or physically-based models) arose because all GBs were assumed to be opaque in the simulations.

There is ample experimental evidence (presented in the previous chapters of this thesis) indicating that slip transfer through the GBs can take place when there is good alignment between incoming and outgoing slip systems across the boundary. Thus, geometrical criteria based on the orientation of the grains and slip systems across the boundary (Δb, or m') can be used to analyze slip transfer. The effect of these geometrical criteria on slip transfer was included in a physically-based crystal plasticity model used to study stress concentrations in either transparent, translucent, or opaque GBs in bicrystals oriented for single and double slip [76]. The results of the numerical simulations were in good agreement with experimental observations of slip transfer and slip activation on Al GBs, indicating that this approach was able to capture the effect of GBs on the slip behavior of FCC polycrystals.

This strategy is employed in this chapter to determine the flow strength of different FCC polycrystals by means of computational homogenization of an RVE of the microstructure. Different geometrical slip transfer criteria were implemented, and the predictions of the simulations were compared with experimental data in the literature on the Hall-Petch effect in both FCC (Al, Cu, Ni, Ag) and HCP (Ti, Mg) metallic polycrystals. Moreover, the influence of the GB character (either transparent, translucent, or opaque) on the local stresses that may trigger damage was also highlighted.

6.2 Physically-based crystal plasticity model

6.2.1 FCC metallic crystals

The mechanical behavior of the single crystals in the polycrystal is governed by a physically based, rate-dependent crystal plasticity model [78], which was modified to include the effect of slip blocking or transfer between slip systems concurring at a GB [76]. The model was developed within the framework of finite deformations using the multiplicative decomposition of the deformation gradient, following standard crystal plasticity implementations [158].

The relationship between the plastic shear deformation rate in the slip system α, $\dot{\gamma}^{\alpha}$, and the corresponding resolved shear stress, τ^{α}, is expressed by

$$\dot{\gamma^{\alpha}} = \dot{\gamma_0} \left(\frac{|\tau^{\alpha}|}{\tau_c^{\alpha}} \right)^{\frac{1}{m}} sgn(\tau^{\alpha}) \tag{6.2}$$

where $\dot{\gamma_0}$ is the reference shear strain rate, m the strain rate sensitivity parameter, and ${\tau_c}^{\alpha}$ is the CRSS in the slip system α. Standard values of $\dot{\gamma_0}$ and m for FCC polycrystals can be found in Table 6.1 [78].

The evolution of the CRSS during deformation follows a particularization of the Taylor model [175] by Franciosi *et al.* [57], which includes the contribution between dislocations in different slip systems to the hardening according to

$$\tau_c^{\alpha} = \mu b \sqrt{\sum_{\beta} q^{\alpha\beta} \rho^{\beta}} \tag{6.3}$$

where μ, b, and ρ^{β} stand for the shear modulus parallel to the slip plane, the Burgers vector, and the dislocation density in slip system β, respectively. The dimensionless coefficients $q^{\alpha\beta}$ stand for the different interactions between pairs of slip systems and were obtained by means of discrete dislocation dynamics simulations for FCC lattices where dislocation slip occurs in 12 {111}<110> systems [22, 44]. Due to symmetry considerations, only six independent coefficients are necessary to determine the 12 $\times$ 12 coefficients of $q^{\alpha\beta}$, and they are depicted in Table 6.1.

Table 6.1: Parameters of the dislocation-based crystal plasticity model for FCC single crystals.

Viscoplastic parameters	
Reference shear strain rate $\dot{\gamma_0}$ (s^{-1})	0.001
Strain rate sensitivity coefficient m	0.05
Dislocation interaction coefficients ($q^{\alpha\beta}$)	
Self interaction	0.122
Coplanar interaction	0.122
Collinear interaction	0.657
Glissile junction	0.137
Hirth lock	0.084
Lomer-Cottrell lock	0.118

The evolution of the dislocation density in each slip system, $\dot{\rho^{\alpha}}$, follows the Kocks-Mecking law [97, 98] that takes into account the balance between the generation and annihilation of dislocations. Nevertheless, the original idea of Kocks-Mecking was modified by Haouala *et al.* [76] to account for the formation of dislocation pile-ups in the slip system near a GB that does not allow for slip transfer leading to

$$\dot{\rho}^{\alpha} = \frac{1}{b}\left(\frac{1}{\ell^{\alpha}} - 2y_c\rho^{\alpha}\right)|\dot{\gamma}^{\alpha}| \quad \text{if slip transfer is allowed for any } \beta \tag{6.4}$$

$$\dot{\rho}^{\alpha} = \frac{1}{b}\left(\max\left(\frac{1}{\ell^{\alpha}}, \frac{K_s}{d_b}\right) - 2y_c\rho^{\alpha}\right)|\dot{\gamma}^{\alpha}| \text{ if slip transfer is blocked } \forall\beta \tag{6.5}$$

where β stands for any slip system in the nearest neighbor grain. Eq. 6.4 stands for the standard Kock-Mecking law that includes two terms that control the generation and annihilation of dislocations. Dislocation generation in the slip system α depends on the dislocation Mean Free Path (MFP), ℓ^{α}, which stands for the distance traveled by a dislocation segment before it is stopped by an obstacle, and it is given by

$$\ell^{\alpha} = \frac{K}{\sqrt{\sum_{\beta\neq\alpha}\rho^{\beta}}} \tag{6.6}$$

where ρ^{β} is the dislocation density in the slip system β and K is a dimensionless constant, known as the similitude coefficient, that relates the flow stress with the average wavelength of the characteristic dislocation pattern. It was estimated by Sauzay *et al.* [155] and Rubio *et al.* [151] for different FCC polycrystals.

Dislocation annihilation is controlled by the current dislocation density in the system α and y_c, the effective annihilation distance between dislocations. This latter parameter was estimated for different FCC metals [151], assuming equal densities of edge and screw dislocations. The annihilation distance for edge dislocations y_e is very small ($\approx 6b$) and independent of the metal, while that for screw dislocations y_s is a function of the stacking fault energy, temperature, and strain rate [51, 100]. The values of the critical annihilation distance for screw dislocations are taken from experimental investigations for Cu and Al [8, 100] and from dislocation dynamics simulations for Ni and Ag [141]. Assuming an equal fraction of edge and screw dislocations, the effective annihilation distance y_c is calculated as the average between y_e and y_s.

Eq. 6.4 establishes the dislocation accumulation rate at any slip system in any Gauss point of the polycrystal that is either far away from any GB boundary or when -even if the Gauss point is close to a GB- slip transfer to another slip system β is possible across the GB according to a geometrical criteria that has to be defined.

In contrast, Eq. 6.5 provides the dislocation accumulation rate for a slip system at a Gauss point near a GB when slip transfer across the boundary is blocked according to the geometrical criteria. The critical distance at the GB that leads to an increase in the dislocation generation rate (and, thus, to the formation of a dislocation pile-up) is given by the condition $K_s/d_b > 1/\sqrt{\ell^{\alpha}}$ where K_s is another dimensionless constant that determines the storage of dislocations at the GB and d_b is the distance from the Gauss point to the nearest GB along the slip direction. K_s was also determined by means of 3D dislocation dynamics simulations in the presence of impenetrable grain boundaries in FCC polycrystals [153] while d_b depends on the location of the Gauss point and on the orientation of the crystal.

The different coefficients of the crystal plasticity model for FCC Al, Ni, Cu, and Ag, as well as the elastic constants, are depicted in Table 6.2.

Table 6.2: Parameters of the dislocation-based crystal plasticity model for FCC materials [78, 151]

	Cu	Al	Ni	Ag
Elastic constants (GPa)				
C_{11}	168.4	108	249	124
C_{12}	121.4	61.3	155	93.7
C_{44}	75.4	28.5	114	46.1
Shear modulus μ	30.5	25.0	58.4	19.5
Dislocation parameters				
Burgers vector b (nm)	0.256	0.286	0.250	0.288
Effective annihilation distance y_c (nm)	15	56	14	12.5
Dislocation storage coefficient K	6	9	11	5
Grain boundary storage coefficient K_s	5	5	5	5

6.2.2 HCP metallic crystals

The physically-based crystal plasticity model for FCC metals presented in Section 6.2.1 was extended to HCP metallic crystals, namely Ti and Mg. To this end, the different slip systems active during the plastic deformation of HCP crystals have to be included in the model. Following Table 1.2, they are three (0001) basal slip systems and three $\{10\bar{1}0\}$ prismatic slip systems for both Ti and Mg, plus twelve first-order pyramidal $\{10\bar{1}1\}$ slip systems for Ti, and six second-order pyramidal $\{10\bar{2}2\}$ slip systems for Mg. Thus, there are 18 different slip systems in Ti and 12 in Mg that can be categorized into three families: basal, prismatic, and pyramidal (I or II). It should be noted that deformation twinning is another important plastic deformation mechanism in HCP metallic crystals, particularly in Mg, but it will not be included in this implementation. Thus, the comparison of the simulations for the Hall-Petch effect with experimental data in Ti and Mg will be carried out under conditions where deformation twinning can be neglected, such as high temperature and low strain rates [34].

The c/a ratio (that determines the orientation of the pyramidal slip planes as well as the distance between compact hexagonal planes) and the elastic constants of Ti and Mg single crystals used in the crystal plasticity model are shown in Table 6.3. $c/a \sim 1.63$ in pure Mg and the CRSS for basal slip is very low because the basal planes are the most compact ones. Conversely, $c/a < 1.63$ in Ti and prismatic glide will be dominant with respect to basal slip [106].

Table 6.3: Parameters of the dislocation-based crystal plasticity model for Ti and Mg (HCP) single crystals. The values of the stiffness constants (expressed in GPa) are taken from [81] for Ti and from [194], whereas the values of c/a are taken from [128] for Ti and from [23] for Mg.

	Ti	Mg
c/a	1.587	1.633
C_{11}	160	59.4
C_{12}	90	25.6
C_{44}	46.5	16.4
C_{13}	66	21.4
C_{33}	181	61.6
C_{66}	46.5	16.9

The relationship between the plastic shear deformation rate in the slip system α, $\dot{\gamma}^{\alpha}$, and the corresponding resolved shear stress, τ^{α}, can be expressed (as in FCC metals) as

$$\dot{\gamma^{\alpha}} = \dot{\gamma_0} \left(\frac{|\tau^{\alpha}|}{\tau_c^{\alpha}} \right)^{\frac{1}{m}} sgn(\tau^{\alpha}) \tag{6.7}$$

where $\dot{\gamma_0}$ is the reference shear strain rate, m the strain rate sensitivity parameter, and ${\tau_c}^{\alpha}$ is CRSS in the slip system α. Standard values of $\dot{\gamma_0}$ and m for HCP polycrystals can be found in Table 6.4.

Table 6.4: Parameters of the dislocation-based crystal plasticity model for HCP Ti and Mg single crystals.

Viscoplastic parameters	Ti	Mg
Reference shear strain rate $\dot{\gamma_0}$ (s^{-1})	0.001 [37]	0.001 [68]
Strain rate sensitivity coefficient m	0.02 [37]	0.05 [68]
Dislocation interaction coefficients ($q^{\alpha\delta}$)		
Same-hardening [23]	0.15	0.15

The evolution of the CRSS per slip system during deformation (Eq. 6.3) was modified for HCP metals to consider different CRSS for each slip system family as follows,

$$\tau_c^{\alpha} = \tau_{c_0}^{\alpha} + \mu^{\alpha} b^{\alpha} \sqrt{\sum_{\beta} q^{\alpha\beta} \rho^{\beta}}, \tag{6.8}$$

where τ_{c0}^{α} stands for the lattice resistance of the particular slip system family, and μ^{α} and b^{α} are the shear modulus parallel to the slip plane and the Burgers vector of the corresponding slip system family, respectively. It should be noted that the lattice resistance τ_{c0}^{α} of the only slip system family in FCC crystals ({111}<110>) is very small and can be neglected in Eq. 6.3 but this is not the case in HCP crystals. The introduction of different lattice resistances τ_{c0}^{α} for the different slip system families (basal, prismatic, or pyramidal) allows capturing the plastic anisotropy of HCP lattices.

The latent hardening due to the interactions of the dislocations gliding in different slip systems is accounted for through the coefficients of the dislocation interaction matrix $q^{\alpha\beta}$. Bertin *et al.* [23] estimated the 19 different latent-hardening coefficients of the different dislocation interactions in pure Mg, taking into account basal, prismatic, and second-order pyramidal $<c+a>$ slip. However, no information was found for the different dislocation interactions in pure Ti. Given that the active pyramidal slip systems are different for Ti and Mg, it was assumed that the latent hardening parameters were the same for all the dislocation-dislocation interactions in Ti and Mg (see Table 6.4). The influence of this hypothesis on the results was checked in the case of Mg, in which the 19 latent-hardening coefficients are available from [23], and the differences were not relevant.

The shear modulus μ^{α} and the Burgers vector b^{α} per slip system family were found in the literature for Ti and Mg (see Table 6.7). There is, however, no general agreement about the values of the CRSS per slip system because it is very difficult to measure accurately these quantities, and different techniques lead to different results. For instance, compression of single crystal micropillars manufactured by focused ion beam and oriented for single slip has become popular in recent years [67, 94, 152, 180, 181]. However, the small specimen size and the effect of free surfaces induce artifacts that lead to disparities among the results reported in the literature. Conventional slip trace analysis has also been employed to estimate the contribution of different slip systems to the overall plastic deformation in HCP polycrystals [34] but this procedure cannot provide absolute values of the CRSS but the ratios between the different slip system families. Wang *et al.* [183] presented a thorough literature review about the CRSS values and ratios in Ti from different experimental investigations and used high-energy X-ray diffraction microscopy to estimate the CRSS for the different slip systems in pure Ti. However, there is no general agreement in the literature about the actual CRSS for the different slip systems in Ti due to the large scatter in the available data.

Hence, the CRSS per slip system τ_{c0}^{α} is typically treated as a fitting parameter in crystal plasticity models of HCP metals. In this work, the values of τ_{c0}^{α} were fitted to experimental data found in the literature for the flow stress of Ti and Mg as a function of grain size. In the case of pure Ti, the experiments were carried out at room temperature and at $2.8 \cdot 10^{-4}$ s^{-1} for grain sizes from 6 to 100 μm and different applied strains [107]. The experimental data used to fit the CRSS for pure polycrystals Mg with grain sizes in the range 43 to 172 μm were obtained at $200°\mathrm{C}$ and a strain rate of $1.7 \cdot 10^{-4}$ s^{-1} [135]. High temperature was chosen to neglect the effect of deformation twinning, which is not included in the current crystal plasticity model and can have an important effect at room temperature. The fitting process of the lattice resistance τ_{c0}^{α} started by trying to fit the lattice resistance

values of the dominant slip systems, i.e. prismatic slip in Ti and basal slip in Mg. Then, the τ_{c0}^{α} for the other slip systems were chosen in order to keep reasonable CRSS ratios according to the data found in the literature. The results of the flow stress of each set of τ_{c0}^{α} values were validated against the experimental data of flow stress as a function of the grain size, employing the estimated flow stress for a very large grain size. To obtain this value, the intersection of the linear fit of the experimental data with the y-axis was calculated (see Fig. 6.16). This value was compared to the simulation of the polycrystals with fully transparent GBs, that represent the behavior of an "infinite" grain size. The selected values for the CRSS per slip system are shown in Table 6.5, together with the calculated CRSS ratios with respect to prismatic slip for Ti and with respect to basal slip for Mg. These ratios are in agreement with the observed ranges reported by Wang *et al.* [183] for pure Ti, and Chapuis *et al.* [36] and Sánchez-Martín *et al.* [120] for pure Mg at high temperature.

Table 6.5: Lattice resistance and CRSS values for the Ti and Mg polycrystals, calculated with Eq. 6.8. The CRSS ratios with respect to prismatic slip are indicated between parenthesis for Ti, and the CRSS ratios with respect to basal slip are indicated between parenthesis for Mg.

	Ti			Mg		
	basal	*prism*	*pyr (I)*	*basal*	*prism*	*pyr (II)*
Lattice resistance $\tau_{c_0}^{\alpha}$ (MPa)	52.9	24.4	76.3	0	10	25
CRSS τ_c^{α} (MPa)	60 (2)	30	90 (3)	0.7	10.7 (15)	26.3 (38)

The modified Kocks-Mecking law that controls the evolution of dislocation density (Eqs. 6.4 and 6.5) during deformation in HCP metals is equivalent to the one in FCC metals,

$$\dot{\rho}^{\alpha} = \frac{1}{b^{\alpha}}\left(\frac{1}{\ell^{\alpha}} - 2y_c^{\alpha}\rho^{\alpha}\right)|\dot{\gamma}^{\alpha}| \quad \text{if slip transfer is allowed for any } \beta \tag{6.9}$$

$$\dot{\rho}^{\alpha} = \frac{1}{b^{\alpha}}\left(\max\left(\frac{1}{\ell^{\alpha}}, \frac{K_s}{d_b}\right) - 2y_c^{\alpha}\rho^{\alpha}\right)|\dot{\gamma}^{\alpha}| \quad \text{if slip transfer is blocked } \forall\beta, \tag{6.10}$$

where β stands for any slip system in the nearest neighbor grain. Eq. 6.9 stands for the standard Kock-Mecking law that includes two terms that control the generation and annihilation of dislocations. Dislocation generation in the slip system α depends on the dislocation MFP, ℓ^{α} given by Eq. 6.6, where K was estimated by Alankar *et al.* [6] for α-Ti. No information was found about K for pure Mg was found in the literature, and the value for Ti was used.

Dislocation annihilation is controlled by the current dislocation density in the system α ρ^{α} and y_c^{α}, which stands for the effective annihilation distance between dislocations for the current slip system family. The critical annihilation distance for screw dislocations y_{edge}^{α} is estimated as $6b^{\alpha}$, as in FCC polycrystals. In the case of screw dislocations, Essmann *et al.* [51] proposed a relation between the critical annihilation distance and the CRSS for

dislocation glide. The assumption is that, in the absence of external stresses, two screw dislocations of opposite sign, separated by a distance y_c, experience an attractive shear stress of $\mu b/2\pi y_c$, where μ is the shear modulus and b the magnitude of the Burgers vector. These dislocations will mutually annihilate if the stress exceeds the stress τ_c required for dislocation glide, i.e. the CRSS. Hence, the critical dislocation annihilation distance assuming equal densities of edge and screw dislocations can be calculated according to

$$2y_c^\alpha = y_e^\alpha + y_s^\alpha = 6b^\alpha + \frac{\mu^\alpha b^\alpha}{2\pi\tau_c^\alpha}, \tag{6.11}$$

where the shear modulus μ^α, the Burgers vector b^α, and the CRSS τ_c^α depend on the slip system. In HCP metals, cross-slip can take place between <a> dislocations gliding in the basal and the prismatic slip planes. Hence, the smallest y_c^α among basal and prismatic slip is imposed for both slip system families because cross slip is controlled by the slip system with the highest CRSS (and, thus, the smallest y_c). The calculated values of y_c^α for each slip system family are presented in Table 6.6, and the smallest y_c between <a> basal and prismatic slip are chosen and highlighted in bold.

Table 6.6: Calculated and chosen critical annihilation distance between dislocations y_c^α for the Ti and Mg polycrystals, calculated with Eq. 6.11. The smallest y_c^α among basal and prismatic slip is highlighted in bold and will be chosen for both slip systems to account for basal-prismatic cross-slip.

	Ti			Mg		
	basal	*prism*	*pyr (I)*	*basal*	*prism*	*pyr (II)*
Calculated y_c^α (nm)	**19**	29	26	840	**40**	32
Chosen y_c^α (nm)	19	19	26	40	40	32

Eq. 6.10 provides the dislocation accumulation rate for a slip system at a Gauss point near a GB when slip transfer across the boundary is blocked. The critical distance at the GB that leads to an increase in the dislocation generation rate (and, thus, to the formation of a dislocation pile-up) is given by the condition $K_s/d_b > 1/\sqrt{\ell^\alpha}$. Due to the lack of information about K_s for HCP polycrystals, it was assumed to be the same used for FCC polycrystals [153], while d_b depends on the location of the Gauss point and on the orientation of the crystal. The different parameters of the crystal plasticity model for HCP Ti and Mg are included in Table 6.7.

6.3 Polycrystal homogenization framework

6.3.1 RVE generation

The mechanical behavior of polycrystals with different grain sizes was determined by means of the finite element simulation of the deformation of an RVE of the microstructure

Table 6.7: Parameters of the dislocation-based crystal plasticity model depending on the slip systems for the Ti and Mg (HCP) crystals.

	Ti			Mg		
	basal	*prism*	*pyr (I)*	*basal*	*prism*	*pyr (II)*
Shear modulus μ^α (GPa) [23, 81]	46.5	35	47.7	16.4	16.4	16.4
Burgers vector b^α (nm) [23, 128]	2.95	2.95	5.53	3.21	3.21	6.12
Dislocation storage coefficient K [6]	20	20	20	20	20	20
Grain boundary storage coefficient K_s [153]	5	5	5	5	5	5

under uniaxial tension, following the standard procedures in full-field computational homogenization [158].

The RVE was generated using the open-source software Neper [146]. The crystals within the RVE are generated using Laguerre-Voronoi tessellations, which lead to polyhedra with flat interfaces. The generation of the RVE involves three distinct processes: tessellation, meshing, and visualization. The tessellation module constructs the geometry of the polycrystal within a convex domain from user-defined crystal properties. Tessellations can be created from morphological microstructural properties such as grain size and shape. The seeds and weights attributes of the tessellation are set by optimization to obtain the desired cell properties. Crystal orientations can be randomly distributed in the 3D space or directly provided by the user from the information obtained by EBSD or X-ray diffraction. Moreover, RVEs with periodic or non-periodic microstructures can be created.

Once the microstructure has been tessellated, it can be discretized with tetrahedral or hexahedral elements for the finite element simulations using Gmsh [63], either with linear or quadratic interpolation. The discretization approach follows a bottom-up scheme that consists of meshing the 0D, 1D, 2D, and 3D entities (vertices, edges, faces, and polyhedra) successively [146]. Each entity is meshed independently of the other entities of the same dimension to ensure good mesh quality. The mesh properties are controlled by several parameters selected by the user, such as the target characteristic length of the elements, c_l, and the gradient parameter, p_l, which is the maximum ratio between the lengths of two adjacent elements. Finally, the visualization module generates images of both the geometry and the mesh of the created RVE.

The RVE was made up of grains with random crystallographic orientations and discretized with second-order modified tetrahedra (C3D10M elements with ten nodes in Abaqus). The shape of the grains was equiaxed, and the grain size followed a lognormal distribution with average grain size $\bar{D}_g$ and standard deviation of $0.2\bar{D}_g$ (Fig. 6.1).

6.3.2 Boundary conditions

The microstructure of the RVE was periodic along the three directions of the space, and periodic boundary conditions were applied to all the nodes on the boundary of the do-

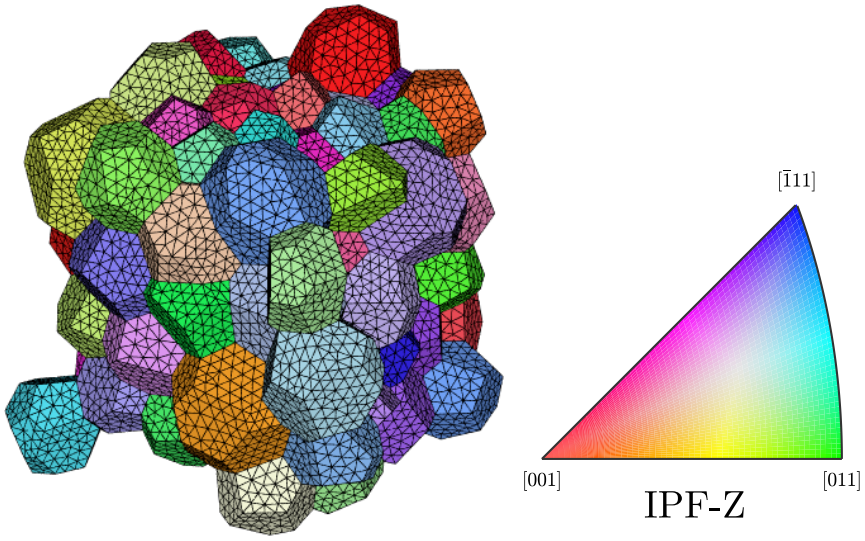

Figure 6.1: RVE of the microstructure including 100 grains discretized with 150000-second order tetrahedra. The grains are colored according to the crystal orientation relative to the Z axis, as indicated in the inverse pole figure.

main. The displacements of each pair of nodes A and B located on opposite surfaces of the domain were linked according to

$$\mathbf{u}_B - \mathbf{u}_A = (\bar{\mathbf{F}} - \mathbf{I})L \tag{6.12}$$

where L is the length of the cubic domain. The far-field deformation gradient $\bar{\mathbf{F}}$ applied to the RVE is obtained by prescribing the displacements of three master nodes M_i.

$$\mathbf{u}(M_i) = (\bar{\mathbf{F}} - \mathbf{I})\mathbf{e}_i \tag{6.13}$$

where $\mathbf{e}_i$ with $i = 1, 2, 3$ stand for the orthogonal basis along the three Cartesian axes x, y, z. The master nodes are linked to the microstructure by three springs of negligible stiffness, joined to a fixed node inside the RVE. The displacement of the master nodes is prescribed by applying a nodal force P_j to the master node M_i and degree of freedom j according to

$$P_j(M_i) = (\bar{\boldsymbol{\sigma}}\mathbf{e}_i)_j A_i \tag{6.14}$$

where $\bar{\boldsymbol{\sigma}}$ is the far-field stress tensor, and A_i is the projection of the current area of the face perpendicular to the $\mathbf{e_i}$ in this direction.

6.3.3 GB distance calculation

In order to apply Eqs. 6.4 and 6.5, it is necessary to calculate the distance d_b from each Gauss integration point to the nearest GB along the slip direction corresponding to each

slip system and to identify the grain across the boundary. This latter information is necessary to apply the geometrical criteria (LRB, m', Δb, or any combination thereof) to assess whether slip transfer across the GB is possible for each slip system. This information only depends on the geometry of the RVE and the discretization, and the values of d_b for each slip system in each Gauss point are calculated and stored before the numerical analysis.

The strategy to determine d_b is schematically presented in Fig. 6.2, which shows a simplified 2D representation of a section of a polycrystal in which grain A is surrounded by grains B, C, and D. The integration point P_0 that belongs to a tetrahedral element of grain A (shaded in grey) is plotted in green in Fig. 6.2 and the slip direction corresponding to the slip system α is plotted as a dashed blue line. The first step to calculate the distance d_b is to identify positions P_0 to P_1 along the positive slip direction (indicated by α^+ in the figure) using the distance $0.5R_{eq}$, where R_{eq} is the equivalent radius of grain A (determined from the volume of the grain assuming that it is spherical). If P_1 belongs to grain A (which is easily determined from the coordinates of the vertices of grain A, which is a convex polyhedron), the process is repeated until the position of P_i is outside grain A and within grain B. Then, a bisection method is used to determine the position of the GB between P_i and P_{i-1} with a given tolerance and to determine d_b along the positive slip direction. The same procedure is repeated for the negative slip direction, and the corresponding distance to the opposite GB, as well as the grain across this boundary, is determined (grain D in this case). The minimum value of d_b from both directions is stored as d_b together with the identifier for the nearest neighbor grain. It was assumed that d_b is constant throughout the analysis, a reasonable assumption because of the small applied far-field strain in the simulations (5%).

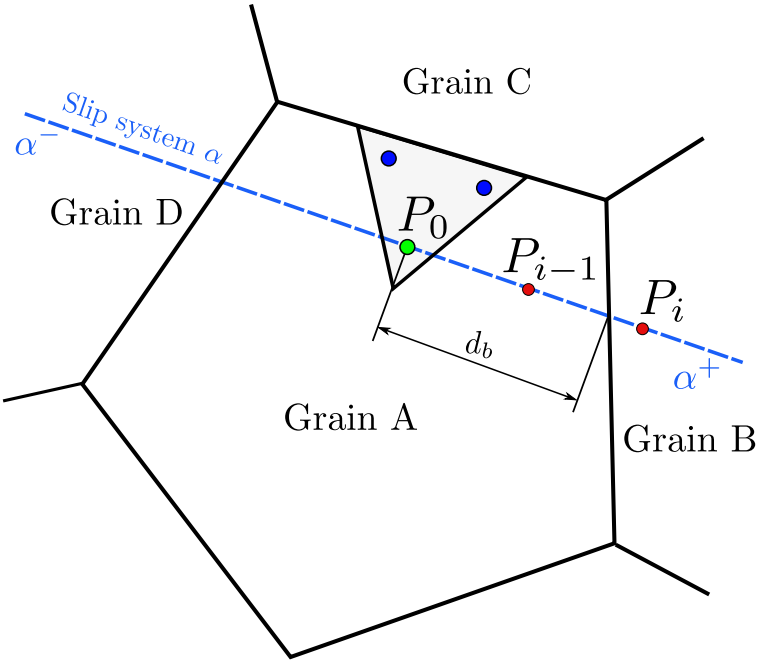

Figure 6.2: Schematic of the calculation of the distance from a Gauss point to the nearest GB along one slip direction.

An exception appears when the integration point is lying next to the outer boundary of the RVE because a point P_i outside the RVE does not lie in the convex hull of any grain. In this case, the grain across the boundary along any slip system has to be determined, taking into account the periodicity of the RVE. The point P_i outside the RVE is shifted in the three directions of the space by a distance $\pm L$, which is the length of the RVE. Because of the periodicity of the RVE, one of the new positions of P_i necessarily falls within one grain, which is the nearest neighbor along such a slip system.

6.3.4 Slip transfer criteria calculation

Once the neighbor grain across the boundary has been identified for each slip system α at each Gauss integration point in grain A, the likelihood of slip transfer from the slip system α in grain A to any of the slip systems β in the neighbor grain B can be assessed using any of the geometrical criteria detailed in the introduction. Two of them, based on the Luster-Morris geometric compatibility criterion m' and on the residual Burgers vector Δb, have been used in this investigation because they are supported by experimental evidence. They can be computed as [19] (Fig. 1.5),

$$m'_{\alpha\beta} = (\boldsymbol{n}_\alpha \cdot \boldsymbol{n}_\beta)(\boldsymbol{b}_\alpha \cdot \boldsymbol{b}_\beta) \quad \text{and} \quad \Delta b_{\alpha\beta} = |\boldsymbol{b}_\alpha - \boldsymbol{b}_\beta| \tag{6.15}$$

where $\boldsymbol{n}_\alpha$ and $\boldsymbol{n}_\alpha$ are unit vectors perpendicular to the slip plane α in grain A and slip plane β in grain B. Obviously, all the vectors in Eq. 6.15 have to be expressed in the same reference frame. The orientation of grain A with respect to the Cartesian reference frame of the RVE is given by the Euler angles (φ_1^A, ϕ^A, φ_2^A) while that of grain B is given by (φ_1^B, ϕ^B, φ_2^B). The vectors $\boldsymbol{n}'_\alpha$ and $\boldsymbol{b}'_\alpha$ expressed in the reference frame of crystal A can be transformed to the reference frame of crystal B, $\boldsymbol{n}_\alpha$ and $\boldsymbol{b}_\alpha$, according to

$$\boldsymbol{n}_\alpha = \boldsymbol{n}'_\alpha \boldsymbol{G}_A^{-1} \boldsymbol{G}_B \quad \text{and} \quad \boldsymbol{b}_\alpha = \boldsymbol{b}'_\alpha \boldsymbol{G}_A^{-1} \boldsymbol{G}_B \tag{6.16}$$

where $\boldsymbol{G}_A$ and $\boldsymbol{G}_B$ stand for the orientation matrices of grains A and B, where, again, orientations are expressed relative to the Cartesian reference frame of the RVE as a function of the Euler angles of each grain, according to [157].

$$\boldsymbol{G} = \begin{pmatrix} \cos\varphi_1 \cos\varphi_2 - \sin\varphi_1 \sin\varphi_2 \cos\phi & \sin\varphi_1 \cos\varphi_2 + \cos\varphi_1 \sin\varphi_2 \cos\phi & \sin\varphi_2 \sin\phi \\ -\cos\varphi_1 \sin\varphi_2 - \sin\varphi_1 \cos\varphi_2 \cos\phi & -\sin\varphi_1 \sin\varphi_2 + \cos\varphi_1 \cos\varphi_2 \cos\phi & \cos\varphi_2 \sin\phi \\ \sin\varphi_1 \sin\phi & -\cos\varphi_1 \sin\phi & \cos\phi \end{pmatrix}.$$

Slip transfer between slip systems α and β is allowed when m' is above (or $\Delta b_{\alpha\beta}$ is below) a threshold value. If the condition of slip transfer is fulfilled for any β slip system in the neighbor grain, Eq. 6.4 is used as the constitutive equation of slip system α at the Gauss integration point of the crystal. Otherwise, slip transfer from α to β is not possible due to the geometric incompatibility, and the constitutive equation is expressed by Eq. 6.5.

It should be noted that these changes in the slip behavior due to the presence of impenetrable GBs are only active near GBs (as dictated by the condition $K_s/d_b > 1/\sqrt{\ell^\alpha}$). Moreover,

the geometrical analysis of slip transfer at each GB indicates how many pairs of slip systems are suitably oriented to transfer slip across the boundary, leading to a classification of GBs from fully opaque (slip transfer is not possible for any pair of slip systems) to translucent (slip transfer is possible for some pairs of slip systems) to fully transparent (slip transfer is allowed for all 12 pairs of slip systems in the case of FCC crystals).

The mechanical behavior of the RVEs under uniaxial tension was simulated using Abaqus Standard [163] within the framework of the finite deformations theory with the initial unstressed state as reference. The constitutive behavior of each crystal was governed by the crystal plasticity model presented in Section 6.2.1, which was implemented in Abaqus through a user-defined material model (UMAT).

6.4 Results and discussion

6.4.1 RVE selection

Different sets of simulations were carried out in FCC Cu RVEs with 20 μm grain size and fully opaque GBs to assess the effect of the number of grains, the discretization, and the random set of orientations on the mechanical behavior of the polycrystals. The mechanical response of RVEs with 50, 100, and 200 grains and random texture was calculated using approximately the same discretization ($\approx$ 50k elements). As shown in Fig. 6.3 (a), the differences in the flow strength between the RVEs with 50 and 100 grains were about 5% and only 2% between the RVEs with 100 and 200 grains. Subsequently, RVEs with 100 grains were discretized with 12000 (coarse mesh), 150000 (medium mesh), and 350000 (fine mesh) second-order tetrahedral elements (C3D10M in Abaqus), to assess the mesh sensitivity in the tensile response of the polycrystals. The coarse discretization overestimated the flow strength of the polycrystal by $\approx$ 10% while the difference in flow strength between the medium and fine discretizations was only 2% (Fig. 6.3 (b)). Thus, RVEs with 100 grains discretized with 150000 elements were selected for the analysis in order to optimize the balance between time and accuracy (final RVE displayed in Fig. 6.1). Finally, simulations of the same RVE with three different sets of random orientations showed differences of 4% between the maximum and minimum flow stress (Fig. 6.3 (c)). Hence, the texture that led to the intermediate flow stress was selected for the simulations presented in this work.

6.4.2 Effect of slip transfer on the flow strength of FCC metals

The effect of grain size and grain boundary character on the mechanical response of Al and Cu polycrystals was analyzed using the crystal plasticity model and the computational homogenization scheme presented above. To this end, RVEs with four different grain sizes $\bar{D}_g$ (10, 20, 40, and 80 μm) and the same set of randomly generated orientations were generated. Simulations were performed at quasi-static strain rates ($\approx 10^{-3}\ s^{-1}$) under uniaxial tension up to 5% applied strain. The initial dislocation density was $\approx 10^{12}$ m^{-2}, evenly distributed among the 12 slip systems, which corresponds to well-annealed

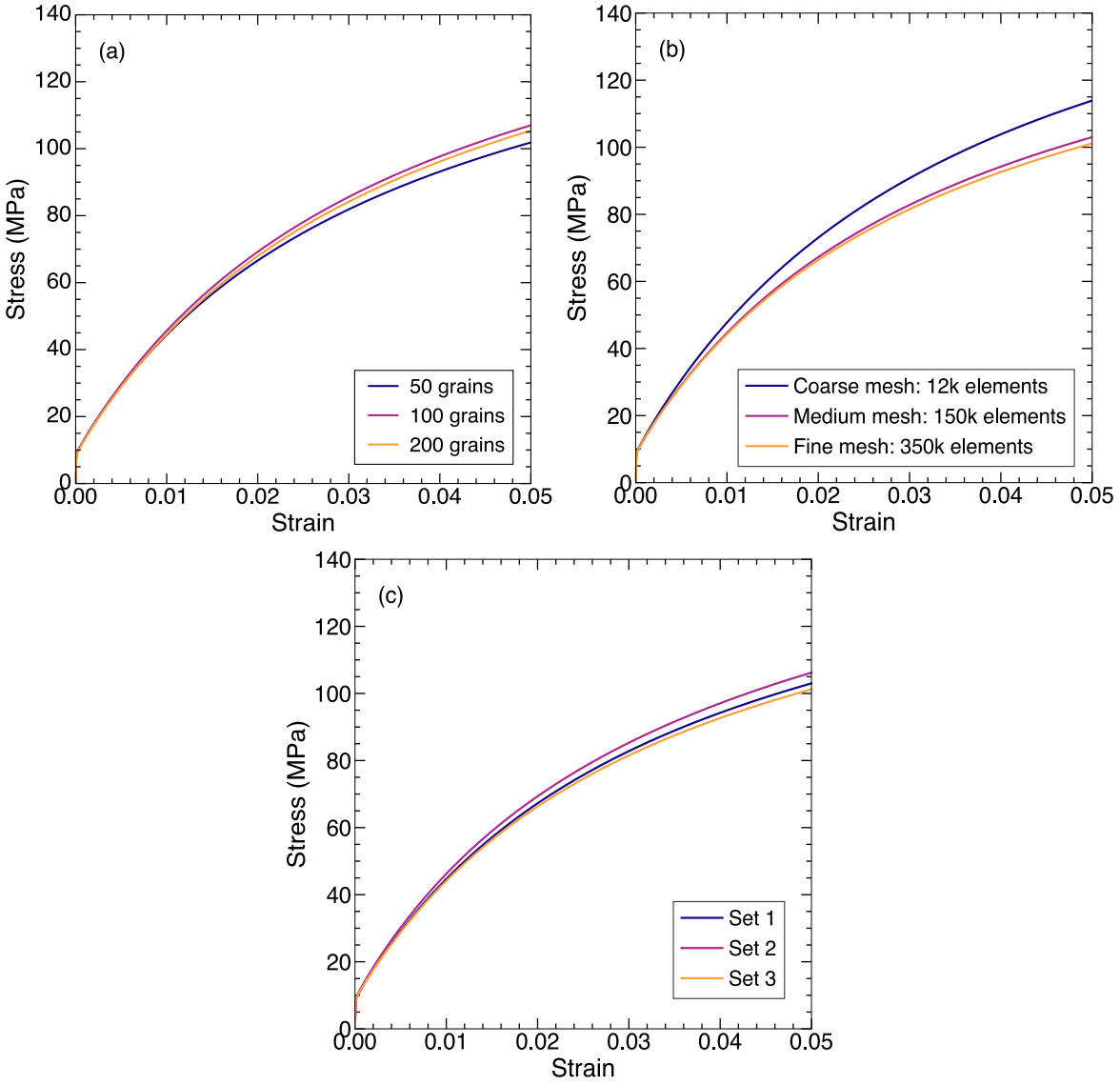

Figure 6.3: RVE selection analysis performed in Cu RVEs with 20 μm grain size and fully opaque GBs. (a) Effect of the number of grains on the tensile response. (b) Effect of the discretization on the tensile response. (c) Effect of the set of random orientations on the tensile response.

polycrystals. The parameters of the crystal plasticity model for both Al and Cu can be found in Tables 6.1 and 6.2.

The effect of grain boundary character on the engineering stress-strain curves under tension of Al and Cu polycrystals with different average grain sizes ($\bar{D}_g$ = 10 μm and 40 μm) is presented in Figs. 6.4 (a)-(d). The stress in these plots has been normalized by μb to reveal the differences in strain hardening between Al and Cu as a result of the interaction, accumulation, and annihilation of dislocations and to compensate for the effect of the differences in elastic constants. Five different curves are plotted in each figure: the strongest

polycrystals correspond to simulations in which all GBs are assumed to be opaque and, thus, the constitutive equation of the material is given by Eq. 6.5. In contrast, the softest response is given by the dashed black curves that were obtained, assuming that all GBs were fully transparent. The constitutive equation of the polycrystal, in this case, is given by Eq. 6.4, and the results of the simulations are independent of $\bar{D}_g$ and stand for the behavior of a polycrystal with an "infinite" grain size. Obviously, the differences in the flow stress between polycrystals with fully opaque and fully transparent GBs increase as the average grain size decreases, in agreement with the Hall-Petch effect. It should be noted that the stress-strain curves of Al polycrystals with either opaque or transparent GBs in Figs. 6.4 (a) and (b) show very little strain hardening for strains $> 2\%$, and this behavior is associated with the high values of K and y_c in the constitutive model. Dislocation multiplication is responsible for the strain hardening in the bulk crystals and decreases as the similitude coefficient K increases because the dislocation MFP is proportional to K. Moreover, dislocation annihilation -which reduces strain hardening- is more efficient for higher y_c. in contrast, the stress-strain curves of Cu polycrystals present continuous strain hardening because K and y_c are smaller. Thus, Al and Cu represent two FCC polycrystals with different strain-hardening behavior.

The three curves between those corresponding to fully opaque and fully transparent GBs in Figs. 6.4 (a)-(d) show the behavior of polycrystals where slip transfer is allowed between slip systems that intersect at a GB when the Luster-Morris parameter m' is higher than a threshold given by 0.9, 0.75 or 0.5. The higher the threshold, the closer the stress-strain curves are to the fully opaque case. On the other hand, the stress-strain curves obtained with a threshold $m' > 0.5$ are almost the same as those obtained with fully transparent GBs for both Al and Cu. The effect of slip transfer on the formation of dislocation pile-ups near the GBs can be ascertained from the spatial distribution plots of the dislocation density in a cross-section of the RVEs corresponding to Al (Figs. 6.5 (a), (c) and (e)) and Cu polycrystals (Fig. 6.5 (b), (d) and (f)) with an average grain size of 10 μm deformed up to 5%. Obviously, high dislocation densities are found at all of GBs if they are assumed to be opaque (Figs. 6.5 (a) and (b)), leading to a large increase in the flow stress observed in Figs. 6.4 (a) and (c) for Al and Cu polycrystals with $\bar{D}_g = 10\ \mu m$. As slip transfer is allowed, some opaque GBs become translucent or transparent as slip transfer is allowed, as shown in Figs. 6.5 (c) and (e) for Al and in (d) and (e) for Cu, and the number of GBs in which dislocation pile-ups have disappeared increases as the geometrical threshold for slip transfer is reduced in the model. In the case of $m' > 0.5$ (not shown in the figure), practically all GBs are transparent, and no dislocation pile-ups can be found.

The formation of pile-ups at GBs is directly associated with an increase in the local stresses, as shown in the spatial distribution plots of the Von Mises stress in the cross-section of the RVEs of Al (Fig. 6.6 (a), (c) and (e)) and Cu polycrystals (Fig. 6.6 (b), (d) and (f)) with an average grain size of 10 μm deformed up to 5%. The more transparent the GB, the lower the stress concentration, and thus, slip transfer may play a dominant role in the determination of the GBs at which damage may develop in polycrystals.

The results presented above show how slip transfer influences the local dislocation density and flow stress at GBs. Obviously, the reduction in the strength of the polycrystal

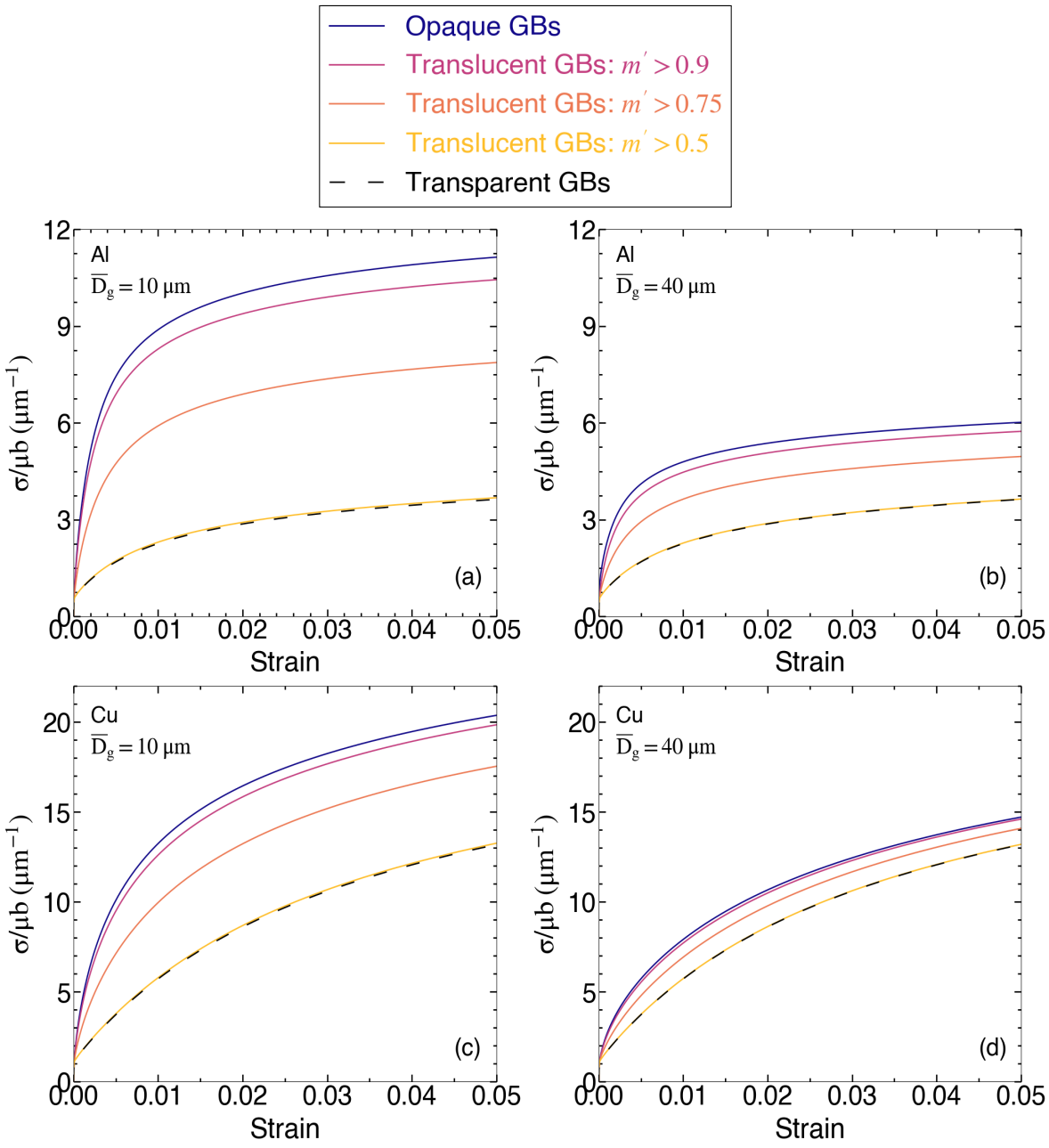

Figure 6.4: Engineering stress-strain curves of Al and Cu polycrystals as a function of grain boundary type: (a) Al $\bar{D}_g$ =10 μm, (b) Al $\bar{D}_g$ = 40 μm, (c) Cu $\bar{D}_g$ = 10 μm and (d) Cu $\bar{D}_g$ = 40 μm.

should be related to the threshold for translucent GBs in the RVE. This information can be obtained from the geometrical analysis to determine the nearest neighbor grain for each slip system α presented in section 6.3 and the corresponding m' values for all the β slip systems in the nearest neighbor grain. Then, a GB between grains A and B is characterized from the viewpoint of slip transfer by all the m' values between all the slip systems in grains A and B. The translucency of the grain boundary can be assessed by analyzing the

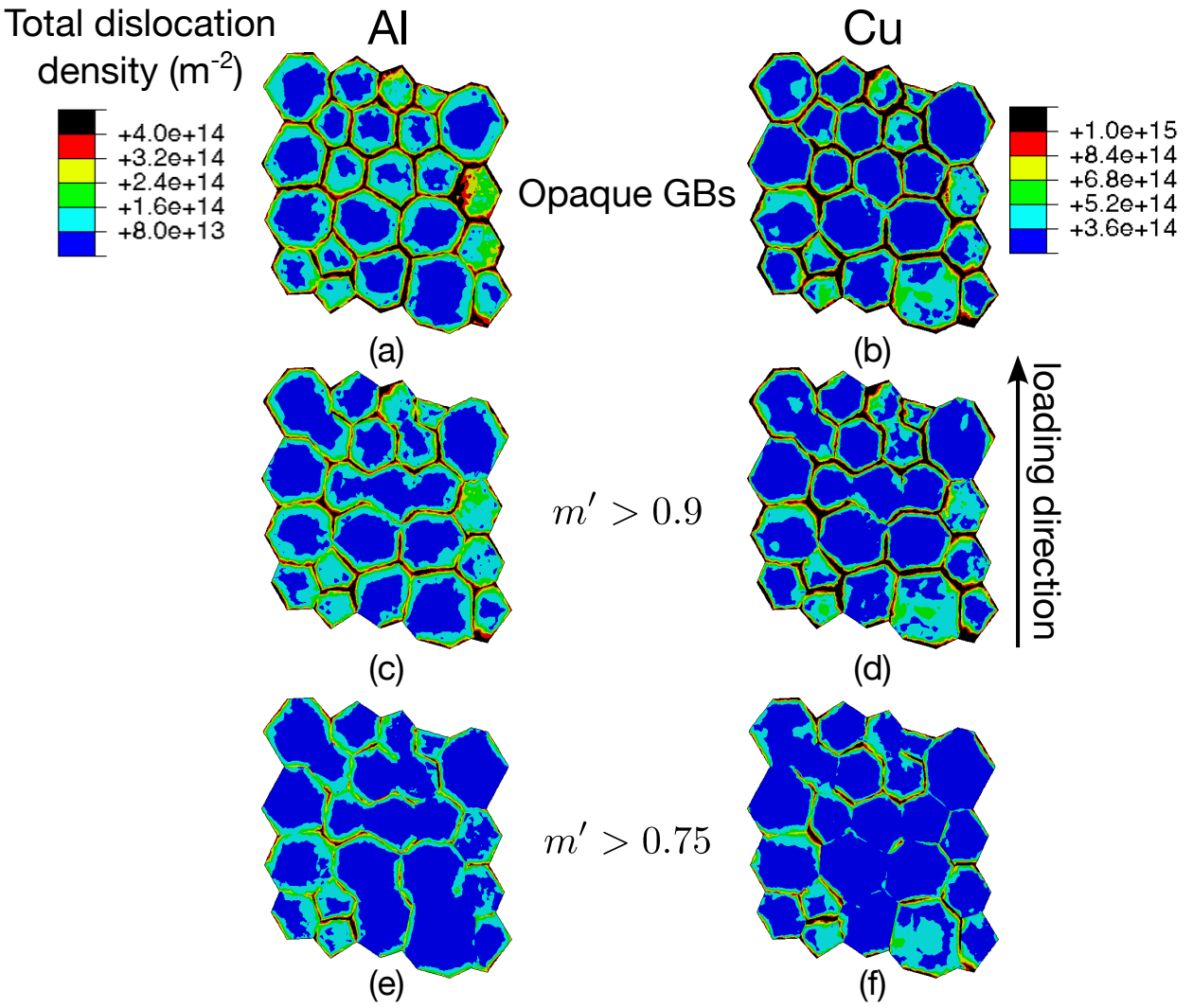

Figure 6.5: Spatial distribution of the total dislocation density (in m^{-2}) in a cross-section of the RVE of the Al and Cu polycrystals with an average grain size of 10 μm deformed up to 5%. (a) Al, opaque GBs. (b) Cu, opaque GBs. (c) Al, translucent GBs with $m' > 0.9$. (d) Cu, translucent GBs with $m' > 0.9$. (e) Al, translucent GBs with $m' > 0.75$. (f) Cu, translucent GBs with $m' > 0.75$.

number of slip systems that fulfill a slip transfer criterion. Taking into account that FCC crystals have 12 slip systems from the $\{111\} < 110 >$ family, a 12×12 m' matrix is calculated for pairs of neighbor grains, where each row relates the geometric compatibility of the lattice from a given incoming slip system α. In this context, slip transfer is considered possible along a certain slip system, for instance, $\alpha = 1$, when any of the $m'_{1\beta}$ values for the 12 possible outgoing slip systems β in the nearest neighbor grain is above the threshold for slip transfer. Thus, the number of slip systems in grain A that can transfer slip can be determined for each grain boundary, and the grain boundaries in the RVE can be classified according to their translucency to dislocations in three distinct groups: opaque GBs (slip transfer is not allowed for any pair of slip systems), translucent or partially-transparent

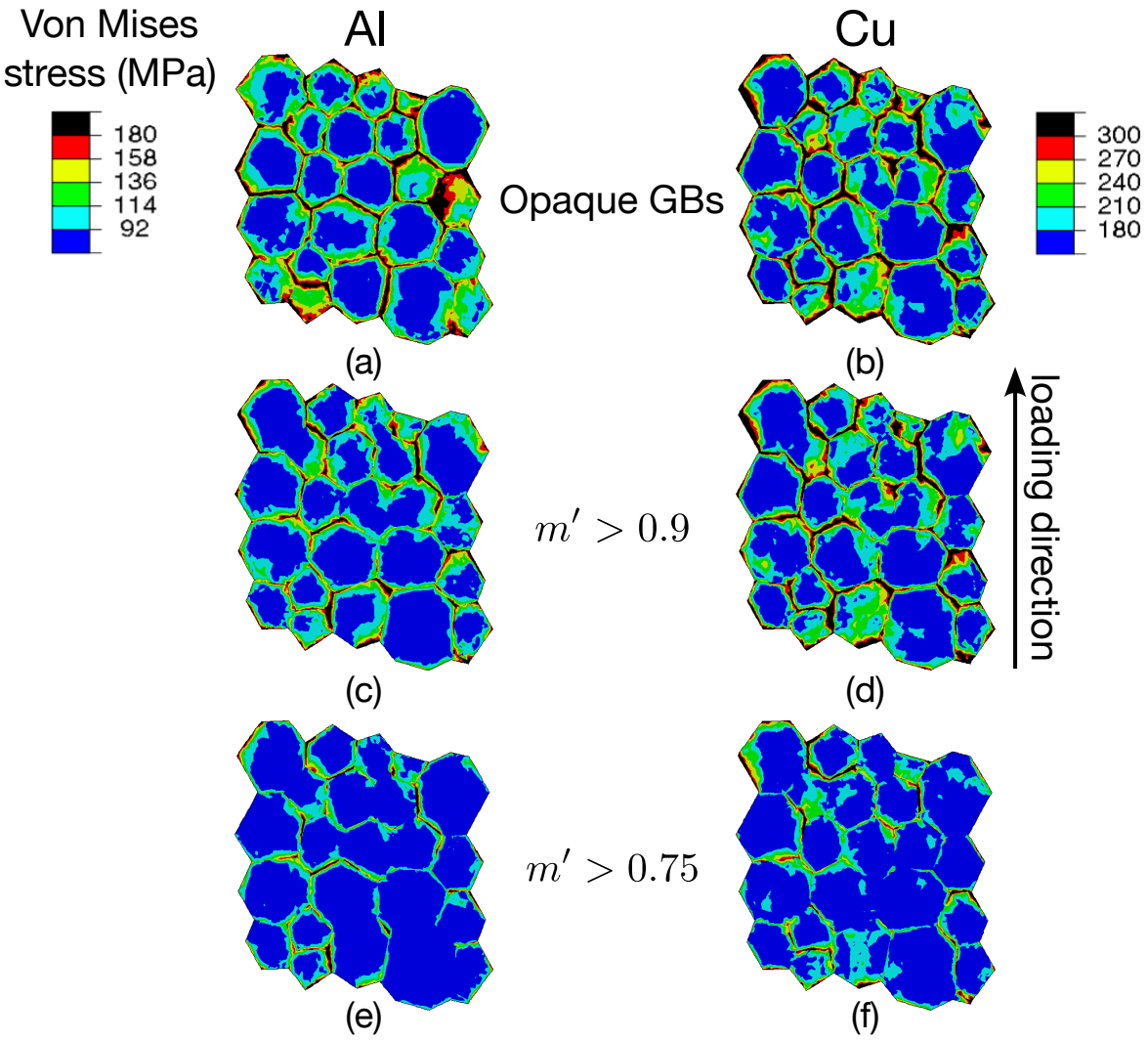

Figure 6.6: Spatial distribution of the Von Mises stress (in MPa) in a cross-section of the RVE of the Al and Cu polycrystals with an average grain size of 10 μm grain size deformed up to 5%. (a) Al, opaque GBs. (b) Cu, opaque GBs. (c) Al, translucent GBs with $m' > 0.9$. (d) Cu, translucent GBs with $m' > 0.9$. (e) Al, translucent GBs with $m' > 0.75$. (f) Cu, translucent GBs with $m' > 0.75$.

GBs (slip transfer is allowed along several pairs of slip systems) and fully transparent GBs (slip transfer is allowed in all slip systems).

The fraction of GBs in the RVE as a function of the number of transparent slip systems across the boundary is plotted in Figs. 6.7 (a) to (c) for different values of the threshold m' for slip transfer. If the threshold for slip transfer is very high, $m' > 0.9$ (Fig. 6.7 (a)), 48% of the GBs are fully opaque while only 3.4% of the GB are fully transparent (all slip systems in one grain can transfer slip to -at least- one slip system in the neighbor grain). Most of the remaining slip systems are translucent and contain 1 to 4 slip systems that can transfer slip to the neighbor grain. The number of GBs where 5 to 11 slip systems can transfer slip is negligible. When the threshold for slip transfer is reduced to $m' > 0.75$, the fraction

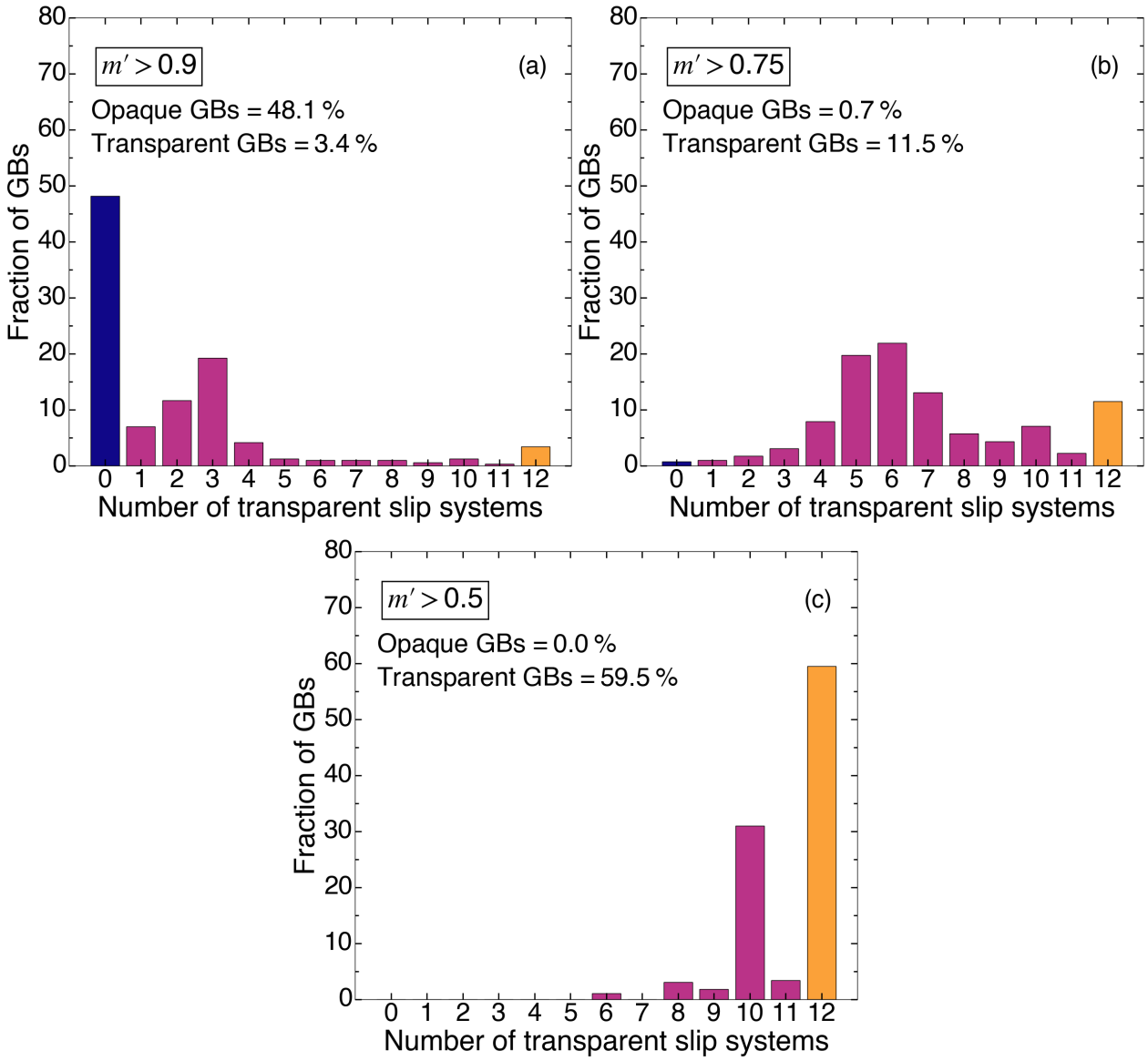

Figure 6.7: Fraction of GBs in the RVE as a function of the number of transparent slip systems. (a) $m' > 0.9$. (b) $m' > 0.75$. (c) $m' > 0.5$.

of fully opaque GBs drops to $< 1\%$ while the number of fully transparent GBs increases to 11.5%. Moreover, most of the GBs can transfer slip across the GB along four or more slip systems. Finally, if the threshold for slip transfer is further reduced to $m' > 0.5$ (Fig. 6.7 (c)), almost 60% of the GBs are fully transparent, and the remaining ones can transfer slip along many slip systems, leading to a polycrystal in which the effect of GBs on the strength can be neglected.

So far, slip transfer in the simulations has been characterized by the Luster-Morris compatibility factor, but any other geometrical factor can be used in the model. For instance, the engineering stress-strain curves for Al and Cu polycrystals with an average grain size of 10 μm are plotted in Figs. 6.8 (a) and (b), respectively, when slip transfer across the

GB was allowed when the residual Burgers vector $\Delta b < 0.45b$. The curves corresponding to fully opaque and fully transparent GBs (as well as those obtained with a slip transfer threshold defined by $m' > 0.75$) are also plotted for comparison. It is worth noting that the stress-strain curves corresponding to $m' > 0.75$ and $\Delta b < 0.45b$ are almost identical for both Al and Cu, suggesting that the reduction in the flow stress due to slip transfer is mainly controlled by the fraction of opaque, translucent and transparent GBs and not by the particular criterion used. This assumption is confirmed by the histograms of the different types of GBs in the RVE from the viewpoint of slip transfer plotted in Fig. 6.9 for both slip transfer thresholds. The fraction of fully opaque and fully transparent GBs is very similar in both cases, and most of the GBs are translucent. Thus, slip transfer is allowed in a wide number of slip systems (from 2 to 10) for both slip transfer thresholds. It is interesting to notice that pairs of slip systems of an FCC crystal share the same Burgers vectors and, thus, the number of transparent or opaque slip systems in the case of the residual Burgers vector criterion is always an even number.

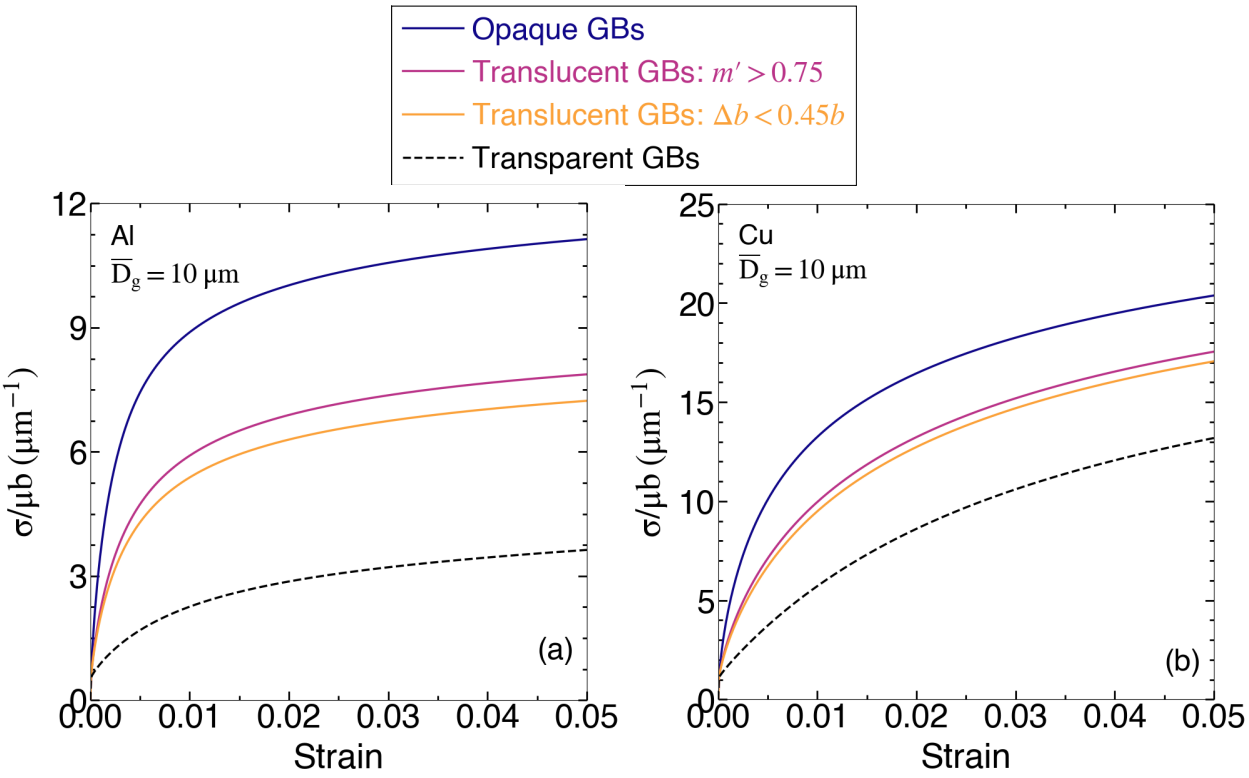

Figure 6.8: Engineering stress-strain curves of polycrystals with an average grain size of 10 μm for opaque and transparent GBs as well as slip transfer criteria of $m' > 0.75$ or $\Delta b < 0.45b$. (a) Al. (b) Cu.

6.4.3 Effect of slip transfer on the Hall-Petch law of FCC metals

The experimental evidence indicates that the strength of polycrystals increases as the grain size decreases following a power-law of the grain size. Based on theoretical results [192]

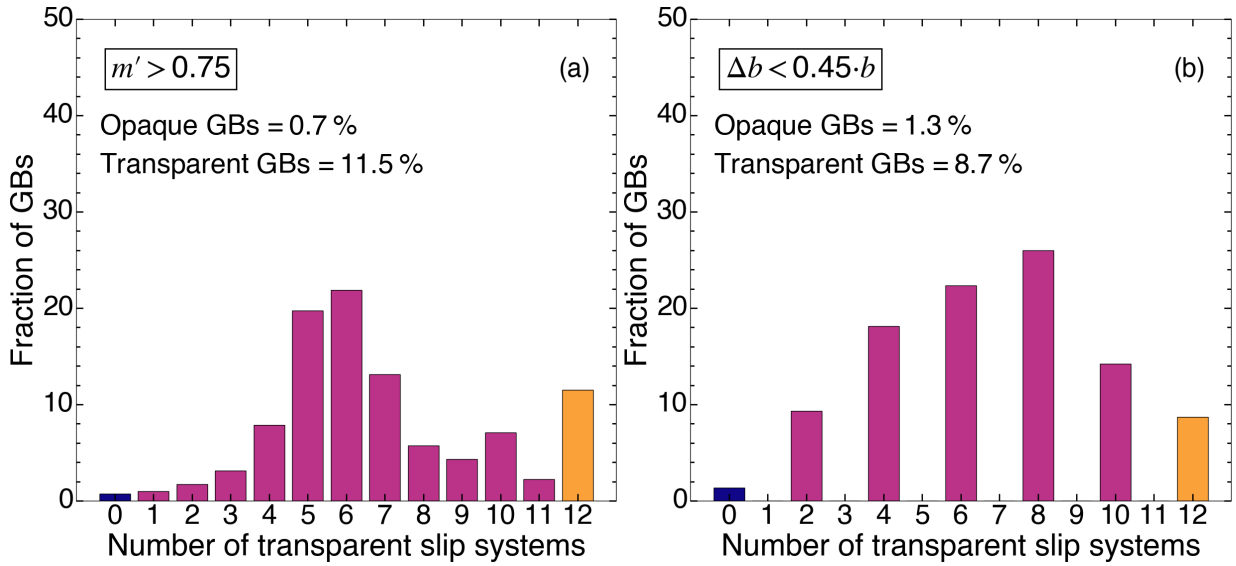

Figure 6.9: Fraction of GBs in the RVE as a function of the number of transparent slip systems. (a) $m' > 0.75$. (b) $\Delta b_{\alpha\beta} < 0.45b$.

and on dislocation dynamics simulations [11], the strengthening caused by GBs, $\sigma_y - \sigma_\infty$, has been proposed to scale with the average grain size $\bar{D}_g$ and the square root of the initial dislocation density in the polycrystal $\sqrt{\rho_i}$ according to [78]

$$\sigma_y/\sigma_\infty - 1 = C(\bar{D}_g\sqrt{\rho_i})^{-x} \tag{6.17}$$

where σ_y is the flow strength of the polycrystal, σ_∞ the flow stress of a polycrystal with "infinite" grain size, and C and x are material constants that depend on the physical parameters of the model for each FCC metal, mainly the similitude constant K and the effective annihilation distance y_c. Eq. 6.17 was in very good agreement with the results of the simulations for Al, Cu, Ni, and Ag FCC polycrystals under the assumption that all GBs were opaque [151] leading to similar values of the exponent (in the range 0.7 to 0.9) when the applied strain was 1%. The effect of slip transfer on the flow strength of Al and Cu polycrystals with different grain sizes (in the range 10 μm to 80 μm) deformed up to ε =1% and 5% is plotted in Fig 6.10. The initial dislocation density in all cases was of the order of 10^{12} m^{-2}.

The results of the simulations show that slip transfer reduces the strengthening provided by GBs but does not modify the exponent of Eq. 6.17 when values of the threshold m' for slip transfer are similar to those reported experimentally [7, 82, 198]. The exponent depends on the FCC metal and on the applied strain. It is slightly lower (more negative) for Cu than for Al and decreases in both cases when the strain to determine the flow strength of the polycrystal is increased from 1% to 5% due to the effect of annihilation of dislocations near the GBs where the dislocation density is maximum. Moreover, the reduction in GB strengthening for Al is always higher than that for Cu when the thresholds for slip transfer are set to $m' > 0.9$ or $m' > 0.75$, although the differences are not huge. They can be attributed to changes in the dislocation accumulation and annihilation of dislocations

near the GBs as a result of the differences in the physical parameters that control these phenomena in each metal.

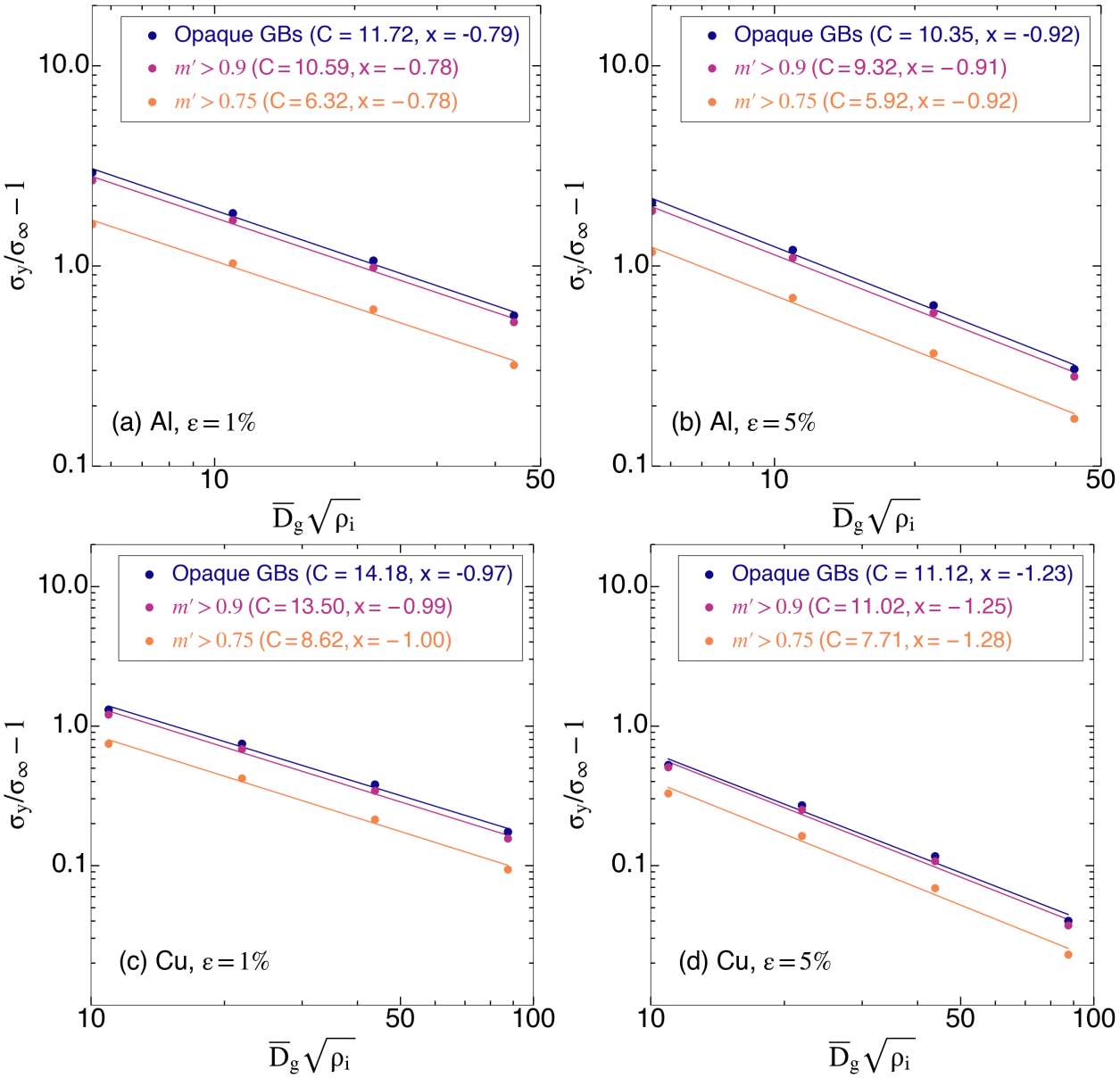

Figure 6.10: Grain boundary strengthening in Al and Cu polycrystals as a function of the adimensional parameter $\bar{D}_g\sqrt{\rho_i}$. (a) Al, $\varepsilon = 1\%$. (b) Al, $\varepsilon = 5\%$. (c) Cu, $\varepsilon = 1\%$. (d) Cu, $\varepsilon = 5\%$. The results of the simulations with fully opaque GBs and with thresholds $m' > 0.9$ and $m' > 0.75$ for slip transfer are plotted in each figure.

6.4.4 Comparison with experiments (FCC)

In order to assess the validity of the modeling strategy presented above, numerical simulations of the flow stress as a function of the grain size were carried out for Al, Cu, Ni,

and Ag polycrystals and compared with experimental data in the literature [33, 74, 75, 127]. The experiments in the literature were carried out at room temperature under quasi-static loading conditions, and, therefore, the effect of the strain rate on the flow stress was considered negligible. Due to the lack of information about the initial experimental dislocation density, it was assumed to be of the order of $10^{12}\ m^{-2}$ in all cases, which is a typical value for well-annealed polycrystals. The parameters of the crystal plasticity model for Al, Cu, Ni, and Ag were obtained by [151] and can be found in Tables 6.1 and 6.2. All the simulations were carried out using the RVE shown in Fig. 6.1 with random texture and average grain sizes in the range 10 μm to 80 μm.

The experimental results of the flow stress in tension are plotted as a function of the inverse of the average grain size, $\bar{D}_g^{-1}$ in Figs. 6.11 (a), (b), (c), and (d) for Al, Cu, Ni, and Ag polycrystals, respectively. Data for two different strain values are shown in each figure. Two simulation results assuming fully opaque GBs (open red circles) and translucent GBs with a threshold for the Luster-Morris parameter (open blue circles) are compared. The thresholds for m' were chosen for each metal to get the best fit of the experimental data because accurate experimental information is unavailable. Nevertheless, they are in the range of the values reported by different experimental investigations of slip transfer [7, 82, 198]. More importantly, good agreement between experiments and simulations is found when the average grain size is large ($\bar{D}_g^{-1} < 25$ mm^{-1}, $\bar{D}_g > 40\ \mu m$), regardless of the inclusion of slip transfer in the simulations, but the trend of the experimental data follows the predictions of the simulations including slip transfer when the grain sizes are smaller than 20 μm ($\bar{D}_g^{-1} > 50$ mm^{-1}). It should be noted, however, that the experimental data set of Ag is smaller than those of Al, Cu, and Ni and presents a larger scatter in the flow stress values, especially for 0.2% applied strain.

The relative errors between the experimental and simulated slopes of the scattered data plotted in Figs. 6.11 (a)-(d) for the studied metals and the different applied strains are displayed in Table 6.8. The relative error assessment shows that, except for the case of Ag at 0.2% strain, the relative error between the translucent GBs simulations and the experimental data is always smaller than that provided by the opaque GBs simulations. Hence, considering the effect of slip transfer in the deformation of polycrystalline materials achieves more realistic results in the tensile response than considering fully opaque GBs. It should be noted that the experimental measurement of the initial dislocation density is complex and time-consuming, usually leading to a lack of information about the dislocation density in the experimental data, which limits the quality of the fittings. This fact, together with the smaller size of the Ag data set, hinders the conclusion that the predictions with translucent GBs are more accurate than those carried out with opaque GBs for Ag at small strains.

It is also important to notice that slip transfer not only influences the overall strength of the polycrystal but also leads to dramatic changes in the stresses at the GBs as a function of the GB orientation (Fig. 6.6). These differences in GBs as a function of orientation are likely to play a dominant role in the nucleation of damage by GB cracking during monotonic and cyclic deformation or in aggressive environments [113, 126] as well as in the development of GB sliding during creep deformation [186]. The combination of the crystal plasticity

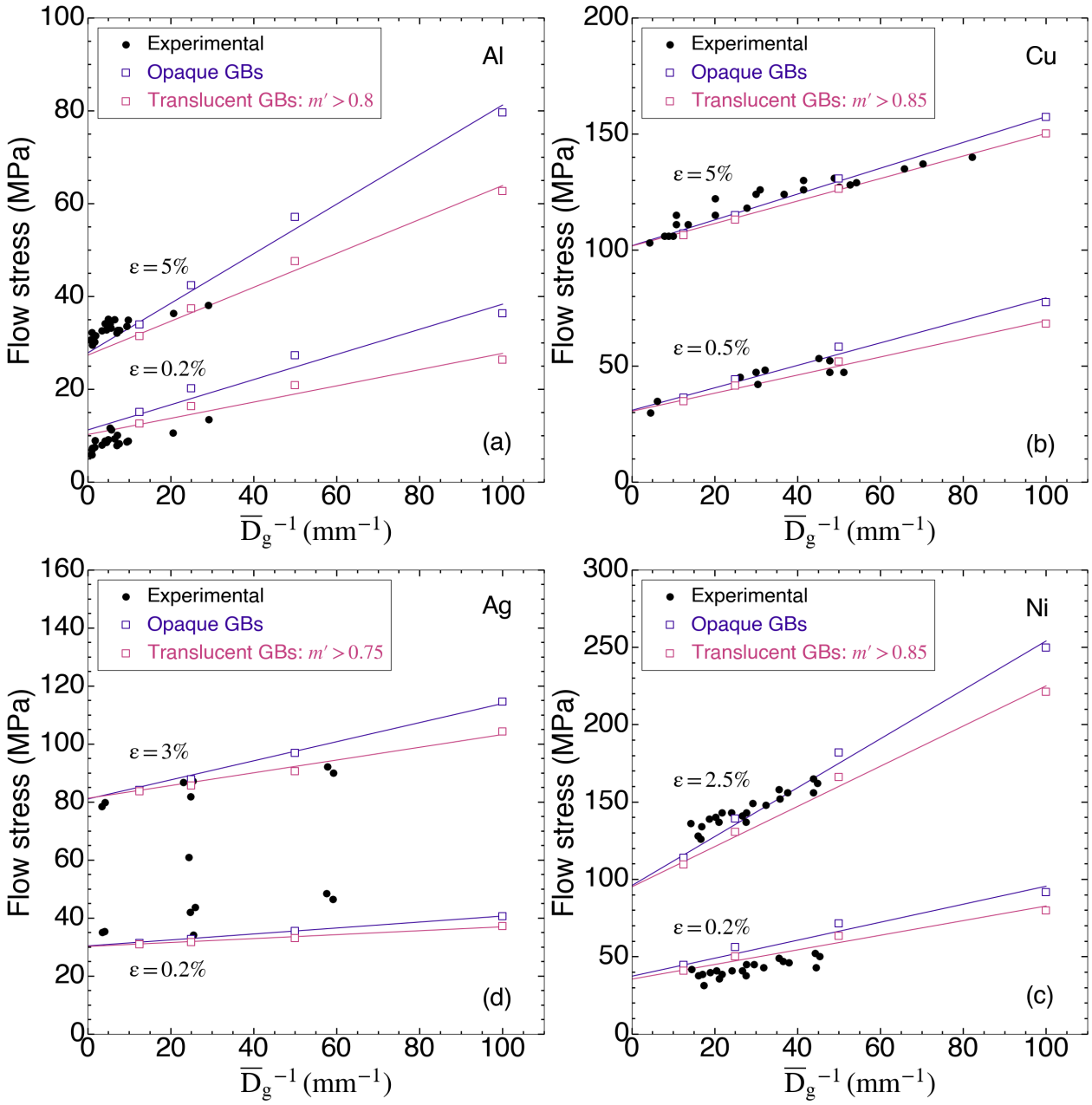

Figure 6.11: Experimental data from the literature and simulation results of the flow stress of Al, Cu, Ni, and Ag polycrystals as a function of $\bar{D}_g^{-1}$ for different applied strains. (a) Al. (b) Cu. (c) Ni. (d) Ag. Experimental results are indicated by black circles, while simulation results without and with slip transfer are represented by open red and blue circles. The linear fittings for the simulated results are indicated in red (opaque GBs) and blue (translucent GBs) solid lines.

model presented in this chapter together with cohesive elements at the GBs [5] would provide a novel way to explore the role of opaque, translucent, and transparent GBs on the ductility, formability, and forming limits of polycrystalline materials.

Material	Strain	m_{exp}	m_{opaque}	$\mathrm{RE}_{\mathrm{opaque}}$	$m_{translucent}$	$\mathrm{RE}_{\mathrm{translucent}}$
Al	0.2%	0.2	0.27	36%	0.18	12.2%
	5%	0.25	0.53	111%	0.37	44.4%
Cu	0.5%	0.39	0.48	22.8%	0.39	1.1%
	5%	0.46	0.56	21.9%	0.49	6.2%
Ag	0.2%	0.2	0.1	47.9%	0.07	65.7%
	3%	0.21	0.33	56.9%	0.22	4.8%
Ni	0.2%	0.41	0.58	42.9%	0.47	16.1%
	2.5%	1.03	1.58	54%	1.3	26.5%

Table 6.8: Flow stress slope error assessment between experimental data and simulation results for different strains for Al, Cu, Ag, and Ni (Fig. 6.11(a)-(d)). m_{exp}, m_{opaque}, and $m_{translucent}$ are the slopes of the scattered data for the experiments, opaque GBs simulation and translucent GBs simulation, respectively. $\mathrm{RE}_{\mathrm{opaque}}$ and $\mathrm{RE}_{\mathrm{translucent}}$ are the relative errors between the experiments and the opaque GBs simulation and between the experiments and the translucent GBs simulation, respectively.

6.4.5 Effect of slip transfer on the flow strength of HCP metals

Numerical simulations of the flow stress as a function of the grain size were carried out for Ti and Mg polycrystals, assuming fully opaque and fully transparent GBs. The same periodic RVE used for FCC polycrystals was employed, with random texture and average grain sizes of 10 μm, 20 μm, 40 μm, and 80 μm (see Fig. 6.1). The simulations were carried out at quasi-static strain rates of $\approx 10^{-4}\ s^{-1}$ to 1% plastic deformation. The initial dislocation density was $\approx 10^{12}\ m^{-2}$, evenly distributed among the slip systems, which corresponds to well-annealed polycrystals. The parameters of the crystal plasticity model adapted for Ti and Mg can be found in Tables 6.3, 6.4, 6.5, 6.6 and 6.7.

The engineering tensile stress-strain curves of Ti and Mg polycrystals up to 1% strain are plotted in Fig. 6.12 as a function of grain size. The simulations with fully opaque GBs are represented by solid lines, and the simulations with transparent GBs are plotted with dashed black lines. The simulations that assume that all GBs are transparent to dislocations are independent of the grain size and stand for the behavior of a polycrystal with an "infinite" grain size. As observed for FCC polycrystals, the differences in the flow stress between polycrystals with fully opaque and fully transparent GBs increase as the average grain size decreases, in agreement with the Hall-Petch effect. The stress in Fig. 6.12 (a) and (b) has been normalized by μb to highlight the differences in the strain hardening rate between Ti and Mg as a result of the interaction, accumulation, and annihilation of dislocations. μ^{prism} and b^{prism} have been used for Ti, whereas μ^{basal} and b^{basal} were used for Mg. This choice is supported by the fact that these slip systems possess the lowest CRSS values and thus will be dominant over the others for the numerical simulations (see Fig. 6.15).

As observed in Fig. 6.12 (d), Mg shows limited strain hardening for strains $> 0.8\%$, and this behavior can be attributed to the higher values of y_c^α in the constitutive model, since dislocation annihilation starts sooner as y_c^α increases. As a result, the dislocation accumulation and annihilation rates tend to balance, and the hardening rate reaches a steady state.

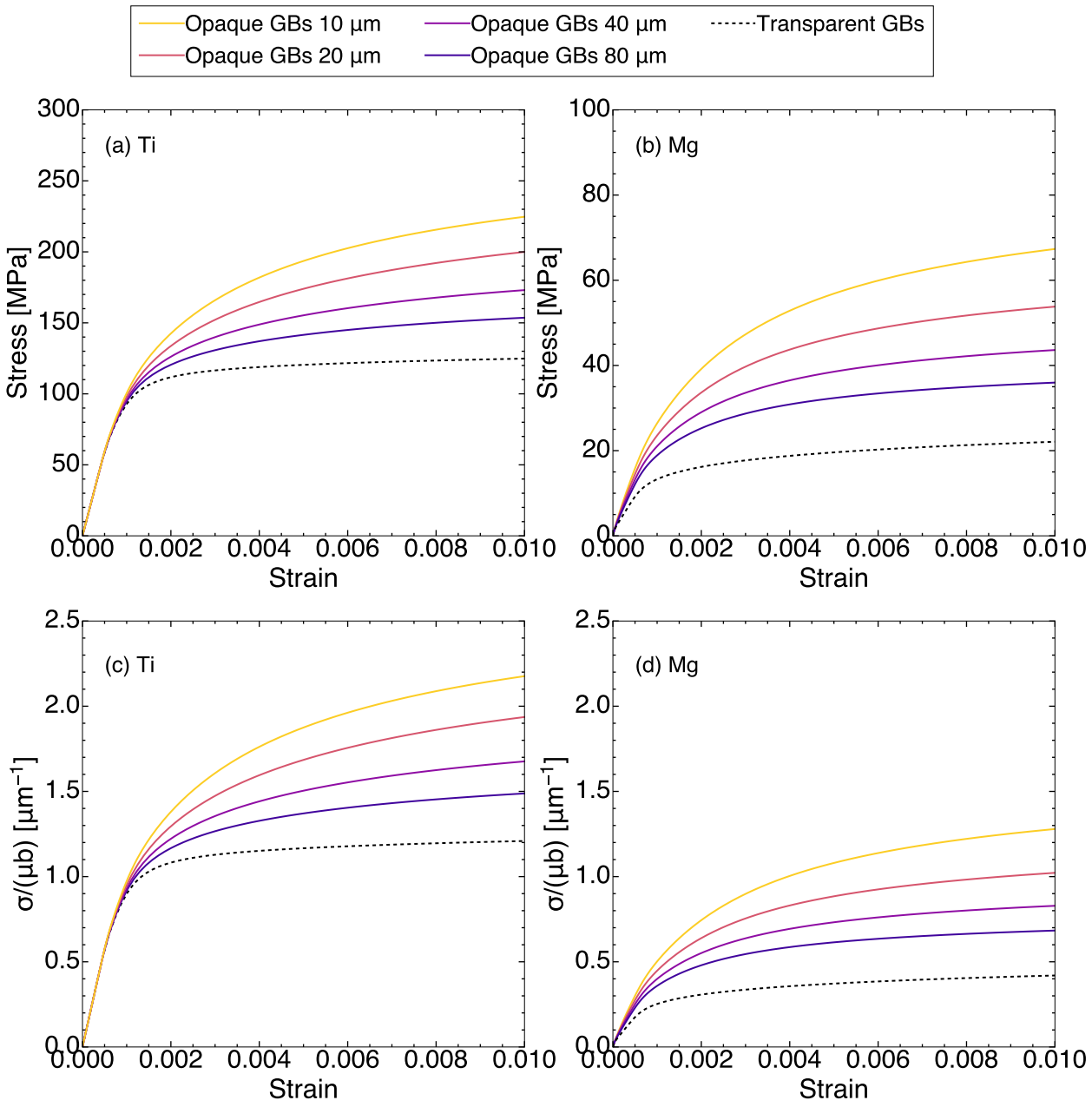

Figure 6.12: Engineering stress-strain curves of polycrystals with transparent GBs and opaque GBs with grain sizes between 10 and 80 μm for (a) Ti, and (b) Mg.

Conversely, the tensile response of Ti still presents strain hardening at 1% because the values of y_c^α are slightly smaller, and dislocation accumulation is dominant over dislocation annihilation.

The spatial distribution of the Von Mises stress (in MPa) and the total dislocation density (in m^{-2}) are plotted Figs. 6.13 and 6.14 for a cross-section of the Ti and Mg RVE polycrystals with transparent and fully-opaque GBs. High dislocation densities are found when GBs are opaque due to the formation of dislocation pile-ups, while smaller dislocation

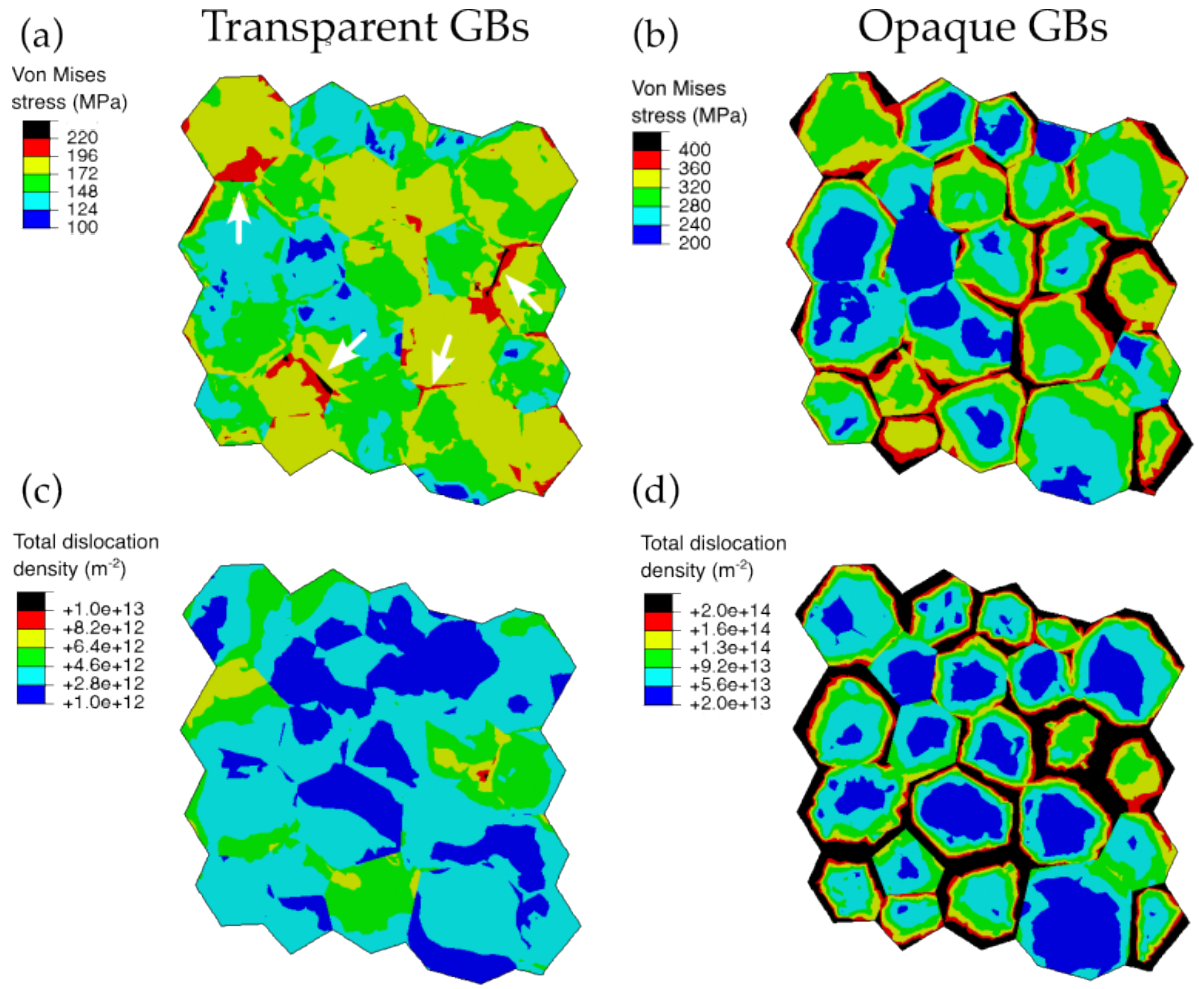

Figure 6.13: Spatial distribution of the Von Mises stress in MPa and the total dislocation density (in m^{-2}) in a cross-section of the Ti polycrystals with transparent GBs (a) and (c), and opaque GBs with an average grain size of 10 μm (b) and (d) deformed up to 1% in tension. Notice the different legend ranges for the stresses and dislocation densities between transparent GBs and opaque GBs. The white arrows in (a) indicate some stress concentrations present at GBs for the simulation with fully transparent GBs.

densities are observed at the bulk of the grains (Figs. 6.13 (d) and 6.14 (d)). However, in contrast to the contour plots obtained for FCC polycrystals (Fig. 6.5 and Fig. 6.6), not all GBs present large dislocation densities despite all GBs being opaque to dislocations. Furthermore, this local increase in dislocation density in some GBs does not necessarily lead to a significant increase in the flow stress, as observed in Figs. 6.13 (b) and 6.14 (b). Instead, the stress is found to be rather homogeneous in some regions, regardless of the location within the bulk of the grain or the GB. This behavior may be attributed to the deformation incompatibility between the grains with different orientations, which is enhanced by the plastic anisotropy of the HCP lattice, where the slip systems contribute differently to plastic deformation. The effect of the plastic anisotropy in HCP metals leads to large variations in the stress fields, which are much larger than in FCC polycrystals. The result is that

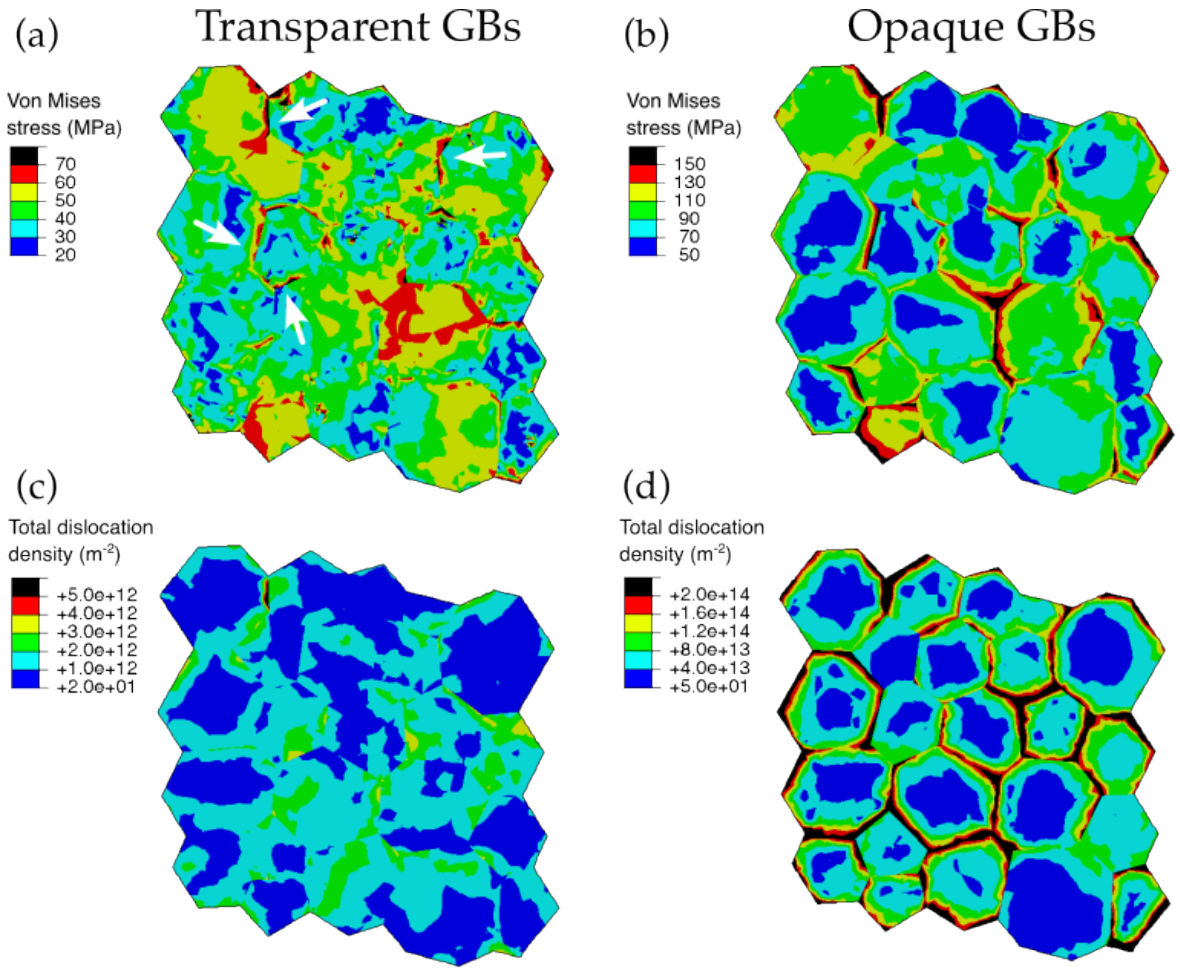

Figure 6.14: Spatial distribution of the Von Mises stress in MPa and the total dislocation density (in m^{-2}) in a cross-section of the Mg polycrystals with transparent GBs (a) and (c), and opaque GBs with an average grain size of 10 μm (b) and (d) deformed up to 1% in tension. Notice the different legend ranges for the stresses and dislocation densities between transparent GBs and opaque GBs. The white arrows in (a) indicate some stress concentrations present at GBs for the simulation with fully transparent GBs.

while some GBs are free of stress concentrations, they are very large in others. In the case of the simulations with transparent GBs, despite GBs not piling up dislocations, there are small stress concentrations observed at a few GBs as compared to the bulk (marked with white arrows in Figs. 6.13 (a) and 6.14 (a)). These stress concentrations are associated with the plastic anisotropy of HCP materials, which leads to deformation incompatibility when deforming grains with different crystal orientations. However, the stresses are generally more homogeneously distributed within the bulk, with some contrasts between adjacent grains, in the simulations with transparent GBs.

The relative activity of slip systems in terms of the accumulated plastic slip γ as a function of the applied strain is shown in Fig. 6.15 for Ti (a) and Mg (b) with 10 μm grain size with fully-opaque (solid lines) and fully transparent GBs (dashed lines). Prismatic slip,

which has the smallest CRSS, presents the greater contribution to plastic slip for the entire simulation, followed by basal and first-order pyramidal slip. The contribution of basal slip increases as the stresses become enough to activate basal slip, whose CRSS is twice that of prismatic slip (Table 6.5). The contribution of the first-order pyramidal slip systems is less than 10% at the end of the simulation, owing to its high CRSS, which is three times that of prismatic slip. The activation of basal slip is delayed in the case of fully transparent GBs in comparison with fully opaque GBs. This effect is caused by the softer tensile response with fully transparent GBs, which leads to lower stresses. Thus, the higher stresses needed to activate basal and pyramidal slip are only reached at higher strains. Conversely, basal slip presents the predominant contribution to γ in Mg (Fig. 6.15 (b)), followed by prismatic and second-order pyramidal, which agrees with the CRSS values set for the simulations. When the GBs are assumed to be fully transparent, the activation of prismatic and pyramidal slip is delayed to higher strains, and their contribution to the accumulated plastic slip is lower.

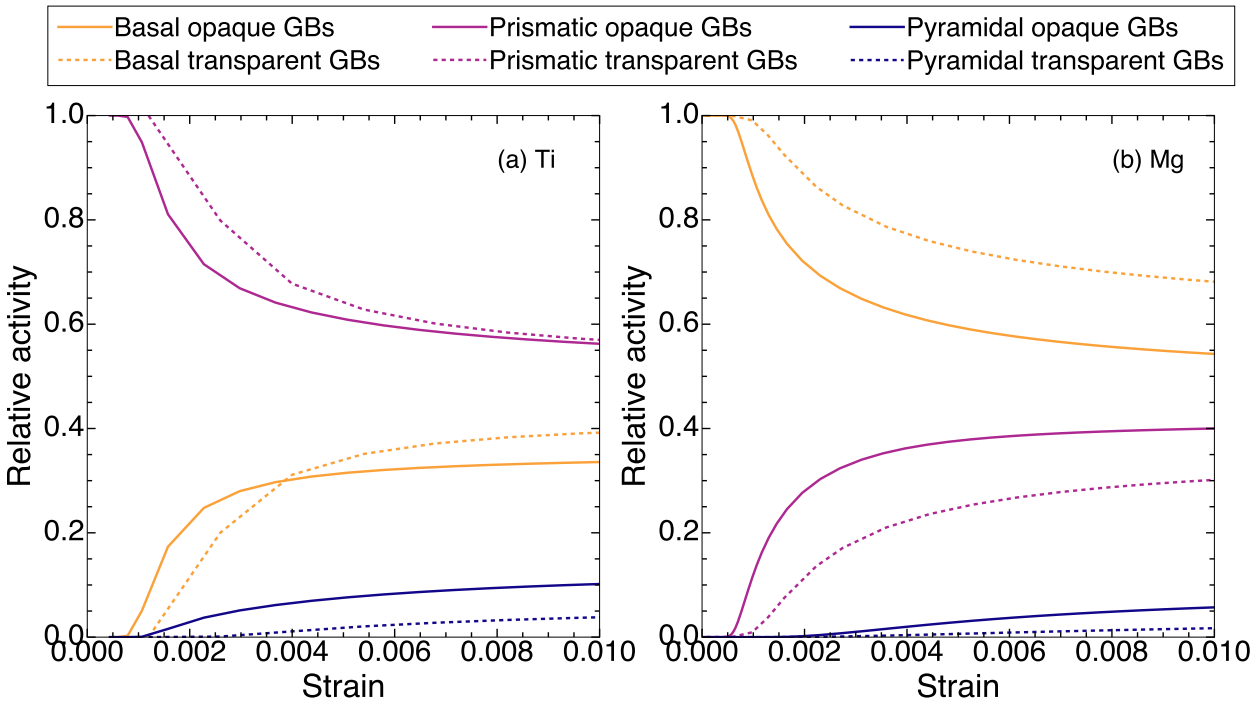

Figure 6.15: Relative activity of the different slip systems to the accumulated plastic slip γ as a function of the applied strain for the 10 μm RVE with opaque GBs and the RVE with transparent GBs for (a) Ti, and (b) Mg.

6.4.6 Comparison with experiments (HCP)

The numerical predictions of the effect of grain size on the flow strength of Ti and Mg were validated against the experimental data found in the literature [107, 135]. The experiments were carried out under quasi-static loading conditions ($\approx 10^{-4}\ s^{-1}$), and, therefore, the effect of the strain rate on the flow stress was considered negligible. The experiments in Ti were carried out at room temperature, while the ones in Mg were performed at $200°C$

[135], where deformation twinning can be neglected. As well as in the case of FCC metals, the dislocation density was assumed to be of the order of $10^{12}\ m^{-2}$ in both cases. The parameters of the crystal plasticity model for Ti and Mg can be found in Tables 6.4, 6.3, 6.5, 6.6 and 6.7. All the simulations were carried out using the periodic RVE shown in Fig. 6.1 with random texture and average grain sizes in the range 10 μm to 80 μm.

The experimental results of the flow stress in tension are plotted as a function of the inverse of the square root of the average grain size, $\bar{D}_g^{-1/2}$ in Figs. 6.16 (a) and (b), for Ti and Mg, respectively. The simulation results assume fully opaque GBs in both cases. The relative errors between the experimental and simulated slopes of the scattered data plotted in Fig. 6.16 (a) and (b) for Ti and Mg for the applied strains are displayed in Table 6.9. The relative error assessment shows that the relative error between the numerical simulations with opaque GBs and the experimental data for the Ti polycrystals at 1% deformation is very small for the fitted CRSS values. The error in the slope is larger in Mg at the yield stress (0.2% deformation), but the lack of information for the flow stress for small grain sizes (< 40 μm) and about the initial dislocation density impedes drawing conclusions about the effect of grain size on the flow stress of Mg. Moreover, slip transfer has not been considered in this model, which could improve the predictions of the flow stress as a function of $\bar{D}_g^{-1/2}$, especially for Mg.

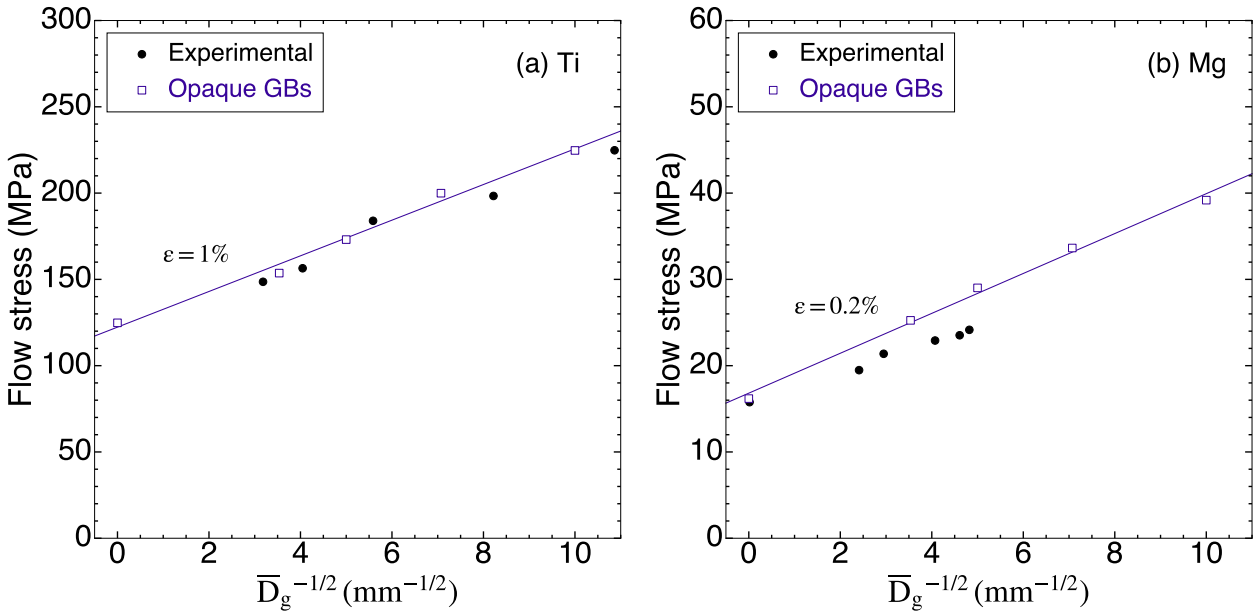

Figure 6.16: Experimental data from the literature and simulation results of the flow stress of HCP polycrystals as a function of $\bar{D}_g^{-1/2}$ for different applied strains for (a) Ti and (b) Mg. The experimental results are indicated by black circles, and simulation results with opaque GBs are indicated by open purple squares. The linear fittings for the simulated results are indicated in purple solid lines.

Material	Strain	m_{exp}	m_{opaque}	$\mathrm{RE}_{\mathrm{opaque}}$
Ti	1%	9.72	10.33	6.3%
Mg	0.2%	1.74	2.31	32.8%

Table 6.9: Flow stress slope error assessment between experimental data and simulation results for different strains for Ti and Mg (Fig. 6.16(a) and (b)). m_{exp} and m_{opaque} are the slopes of the scattered data for the experiments, opaque GBs simulation and translucent GBs simulation, respectively. $\mathrm{RE}_{\mathrm{opaque}}$ is the relative error between the experiments and the opaque GBs simulation.

6.5 Conclusions

The effect of slip transfer on the flow strength of FCC and HCP polycrystals has been analyzed by means of full-field computational homogenization in combination with a physically based crystal plasticity model. The critical resolved shear stress for plastic slip in each slip system follows the modified Taylor model, while the generation and annihilation of dislocations in each slip system in the bulk during deformation is described by a Kocks–Mecking law. This law is modified near the grain boundaries to discriminate between slip systems that can or cannot transfer slip across the boundary using geometrical criteria based on the orientation and activity of the slip systems of both grains near the boundary. This model leads to a classification of the grain boundaries as fully opaque (slip transfer is not possible for any slip system), fully transparent (slip transfer is possible for all slip systems), and translucent (slip transfer is possible for several slip systems). The model was extended to capture the anisotropy of the HCP lattice, including different values for the CRSS for each slip system family (basal, prismatic, and pyramidal).

The mechanical behavior of Al and Cu polycrystals with grain sizes in the range 10 μm to 80 μm and random texture was determined assuming that all grain boundaries were opaque and transparent or that slip transfer was possible for different thresholds of the Luster–Morris geometric compatibility parameter m' or of the residual Burgers vector Δb. Slip transfer between suitably oriented neighbor grains led to a clear reduction in the flow stress of the polycrystals (as compared with the simulations with opaque grain boundaries), which was dependent on the fraction of translucent and transparent grain boundaries in the microstructure, as given by the threshold in the slip transfer geometrical criterion. Moreover, dislocation densities and Von Mises stresses were much higher around opaque grain boundaries, which are potential places for damage nucleation. The strengthening provided by grain boundaries in Al and Cu polycrystals was well described by $C(\bar{D}_g\sqrt{\rho_i})^{-x}$ where $\bar{D}_g$ is the average grain size and ρ_i the initial dislocation density. C depended on the material and on the fraction of translucent and transparent boundaries while x was a function of the material and of the applied strain but was independent of slip transfer at grain boundaries. Finally, the predictions of the simulations were compared with experimental data in the literature on the effect of grain size on the strength of Al, Cu, Ni, and Ag polycrystals. It was found that the inclusion of slip transfer in the model led to more accurate predictions of the Hall–Petch effect, particularly for small grain sizes (< 20 μm).

The crystal plasticity model was extended to HCP metals and employed to carry out numerical simulations of the mechanical behavior of Ti and Mg RVEs under uniaxial tension. The grain boundaries were assumed to be fully opaque and fully transparent to dislocations. The effect of the grain size on the flow stress was accurately captured for both Ti and Mg, which presented different strain hardening behaviors due to the difference between the dislocation annihilation distance. The spatial distribution of the Von Mises stress and the total dislocation density stress concentrations at the GBs were a consequence in HCP polycrystals of both the formation of dislocation pile-ups and of the accommodation of the deformation between grains with different crystallographic orientations and, thus, large anisotropy in the plastic deformation. The contribution of the different slip systems to the accumulated plastic strain agreed with the CRSS values set for each metal, with prismatic and basal slip being dominant for Ti and Mg, respectively.

Finally, the numerical simulations were validated against experimental data of the flow stress for different grain sizes for conditions where deformation twinning could be neglected. The effect of grain boundaries on the flow stress could be accurately captured for Ti, whereas it was slightly overestimated for Mg. Nevertheless, slip transfer was not accounted for in these simulations, which could improve the agreement with the experimental data, especially for Mg. This fact, together with the lack of data for small grain sizes for the experimental data, impedes drawing conclusions about the effect of GBs on pure Mg. Notwithstanding, the crystal plasticity model efficiently captures the anisotropy existing in the HCP lattice and opens the door to more complex simulations where the effect of the stress concentrations at GBs on damage nucleation is included.